Crystal scale anatomy of a dying supervolcano: an isotope and geochronology study of individual phenocrysts from voluminous rhyolites of the Yellowstone caldera

Kathryn E. Watts · Ilya N. Bindeman · Axel K. Schmitt

Abstract A voluminous (>600 km^3) and long-lived (~520–75 ka) phase of rhyolitic eruptions followed collapse of the Yellowstone caldera 640 ka. Whether these eruptions represent a dying cycle, or the growth of a new magma chamber, remains an important question. We use new U–Th zircon ages and δ^{18}O values determined by ion microprobe, and sanidine Pb isotope ratios determined by laser ablation, to investigate the genesis of voluminous post-caldera rhyolites. The oldest post-caldera rhyolites, erupted between ~520 and 470 ka, exhibit extreme age and oxygen isotopic heterogeneity, requiring derivation from individual parcels of low-δ^{18}O melts. We find a progressive increase in zircon homogeneity for rhyolite eruptions from ~260 to 75 ka, with homogeneous low-δ^{18}O zircon values of 2.7–2.8‰ that are in equilibrium with low-δ^{18}O host melts for the majority of the youngest eruptions. New sanidine Pb isotope data define separate arrays for post-caldera rhyolites and the caldera-forming tuffs that preceded them, indicating that they were not sourced from a mushy Lava Creek Tuff batholith that remained after caldera collapse. Rather, our new age and isotopic data indicate that the post-caldera rhyolites were generated by remelting of a variety of intracaldera source rocks, consisting of pre-Lava Creek Tuff volcanic and plutonic rocks and earlier erupted post-Lava Creek Tuff rhyolites. Batch assembly of low-δ^{18}O melts starting at ~260 ka resulted in progressive homogenization, followed by differentiation and cooling up until the last rhyolite eruption ~75 ka, a trend that we interpret to be characteristic of a dying magma reservoir beneath the Yellowstone caldera.

Keywords Yellowstone · Caldera · Zircon · Rhyolite · Geochronology · Oxygen isotopes · Magma evolution

K. E. Watts (✉) · I. N. Bindeman
Department of Geological Sciences, 1272 University of Oregon, Eugene, OR 97403, USA
e-mail: kwatts@uoregon.edu; kwatts@usgs.gov

A. K. Schmitt
Department of Earth and Space Sciences, University of California, Los Angeles, CA 90095, USA

Introduction

Large caldera volcanoes, or "supervolcanoes," have produced some of the Earth's largest known eruptions of silicic magma. The processes and timescales by which large volumes of silicic magma are generated in the shallow crust, and the petrogenetic paths along which they evolve, whether toward explosive caldera-forming eruptions, effusive lava flows, or stalled plutons and batholiths, are important for hazard and resource assessments for caldera centers worldwide. The advent of microanalytical techniques that enable dating and isotopic measurements of individual crystals has greatly improved our understanding of magmatic systems (see Putirka and Tepley 2008 and references therein) and proven critical to deciphering the complex magmatic histories of caldera volcanoes, where multiple episodes of intrusion, assembly and melt extraction are retained in the crystal record (e.g., Vazquez and Reid 2004; Bacon and Lowenstern 2005; Charlier et al. 2005; Folkes et al. 2011).

One prime example of a caldera complex that has produced large volumes of silicic magma with diverse age and isotopic signatures is the Yellowstone Plateau volcanic field
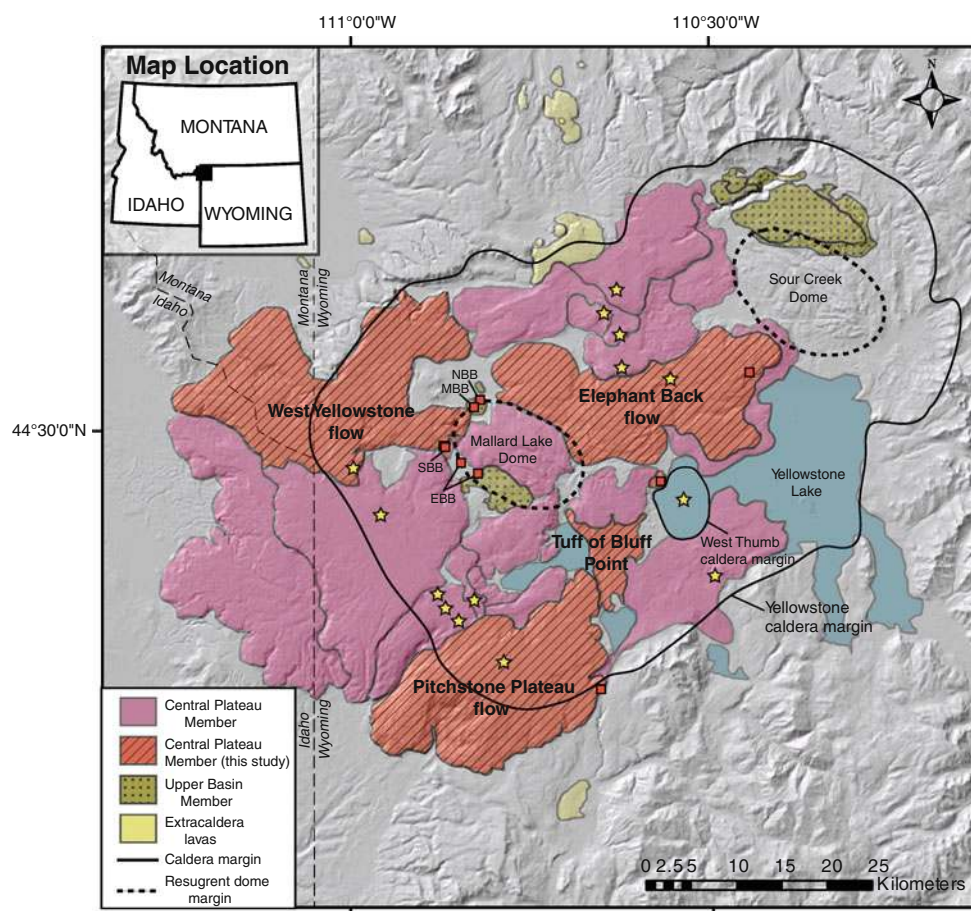
Fig. 1 Map showing the distribution of post-Lava Creek Tuff rhyolites in the Yellowstone caldera. The geologic map of Christiansen (2001) was used to define unit boundaries. The Central Plateau Member units analyzed in this study are indicated by the *bold labels*. *Squares mark* our sampling localities. The locations of the Biscuit Basin rhyolite flows, including North Biscuit Basin (NBB), Middle Biscuit Basin (MBB), South Biscuit Basin (SBB), and East Biscuit Basin (EBB), are also shown. NBB and SBB are Central Plateau Member units, whereas MBB and EBB are Upper Basin Member units (see text for more detail). *Stars mark* the inferred vent sources for individual Central Plateau Member rhyolite eruptions (Christiansen 2001). The Yellowstone caldera margin, resurgent dome margins, and West Thumb caldera margin are taken from Christiansen (2001) and Christiansen et al. (2007). The *inset* shows the map location in the western USA

in western Wyoming (Fig. 1). In this study, we investigate magma genesis during the last caldera-forming cycle at Yellowstone by combining several crystal scale analytical approaches, focusing on dating and isotopic analyses of refractory zircon phenocrysts. Our new results enable us to evaluate whether Yellowstone's youngest episode of rhyolitic volcanism represents a rejuvenating or waning stage of magmatism, using single crystals as probes of magma evolution from the oldest to youngest rhyolite eruptions.

Background

Caldera cycles at Yellowstone

The Yellowstone Plateau volcanic field is the youngest caldera center in the 16-Ma track of the Yellowstone hotspot (Pierce and Morgan 1992). It offers one of the best preserved records of caldera complex evolution above a continental hotspot, with extensive exposures of explosive and effusive deposits from three climactic caldera-forming cycles. These include the 2.06-Ma Huckleberry Ridge Tuff (HRT), 1.29-Ma Mesa Falls Tuff (MFT), and 0.64-Ma Lava Creek Tuff (LCT) (Lanphere et al. 2002). Estimated eruptive volumes for these tuffs are among the largest known for caldera volcanoes, at 2,450, 280, and 1,000 km^3, respectively (Christiansen 2001). Ash fall deposits from the HRT and LCT eruptions once covered much of the North American continent, and the corresponding ash flow tuffs reached thicknesses of up to 500 m near the eruptive vents (Christiansen 2001).

Large caldera-forming eruptions at Yellowstone are bracketed by smaller, predominantly effusive eruptions of pre- and post-caldera lavas. The third LCT caldera cycle

resulted in the formation of the $\sim 70 \times 50$ km Yellowstone caldera, which was subsequently filled by more than 600 km^3 of post-caldera rhyolites that buried most of the caldera floor and the western caldera rim (Fig. 1). Many of these individual lava flows are quite large (>10 km^3) and form well-defined lobate extrusions that cover broad geographic areas of the Yellowstone Plateau volcanic field (Fig. 1). These rhyolites represent either residual magma from the third LCT cycle, or perhaps the beginning of a fourth eruptive cycle, owing to their very large cumulative eruptive volume (Hildreth et al. 1984; Christiansen 2001; Christiansen et al. 2007).

Post-caldera rhyolites of the Yellowstone caldera

Post-caldera rhyolites of the LCT cycle are subdivided into two principal members based on location, age, and composition. The earliest erupted (~ 520–470 ka) rhyolites compose the Upper Basin Member (UBM) flows (~ 50 km^3 total volume) located near the Mallard Lake and Sour Creek resurgent domes of the Yellowstone caldera (Fig. 1). UBM flows have more primitive compositions than younger post-LCT rhyolites (Christiansen et al. 2007; Girard and Stix 2009), and they have the lowest magmatic $\delta^{18}O$ signatures of all studied Yellowstone rhyolites (Hildreth et al. 1984; Bindeman and Valley 2001; Bindeman et al. 2008). Oxygen isotope studies of individual UBM units reveal distinct low-$\delta^{18}O$ obsidian values that range from ~ 0 to 2‰, significant phenocrystic $\delta^{18}O$ heterogeneity spanning an ~ 8‰ range, and zircons with up to 2.1 Ma older cores and inherited (pre-caldera) normal-$\delta^{18}O$ values (Bindeman and Valley 2001; Bindeman et al. 2008). This evidence is taken by the authors to indicate that UBM rhyolite lavas were derived from independent magma batches produced by bulk remelting of hydrothermally altered pre-caldera protoliths.

The youngest (~ 260–75 ka) and most voluminous post-LCT eruptions compose the Central Plateau Member (CPM) units, which consist of at least 17 lava flows and two pyroclastic tuffs (Christiansen et al. 2007). Individual eruptive volumes of CPM rhyolites are typically on the order of ~ 10 km^3, but several approach ~ 50–70 km^3 (Christiansen et al. 2007). The 50-km^3 Tuff of Bluff Point eruption was of sufficient volume and explosivity to generate a smaller caldera within the larger Yellowstone caldera, a ~ 10-km-wide elliptical depression filled by the western portion of the Yellowstone Lake, known as the West Thumb caldera (Fig. 1). CPM rhyolites were erupted in discrete batches from vents along two northwest-striking lineaments that bisect the Yellowstone caldera (Fig. 1). However, the rhyolites display no apparent regional differences in composition for different vent localities (Girard and Stix 2010). Recent studies of several flows previously

recognized as UBM units, including the Scaup Lake, South Biscuit Basin, and North Biscuit Basin flows, demonstrate that they have $\delta^{18}O$ ranges similar to CPM rhyolites and Ar–Ar eruption ages that are ~ 300 ky younger than UBM rhyolites (Christiansen et al. 2007; Bindeman et al. 2008), suggesting that they belong to the CPM rather than UBM group. Here, we include them with the "early" CPM group and suggest that they are important for understanding the more voluminous "later" CPM rhyolites.

Like UBM rhyolites, early CPM units exhibit heterogeneity in zircon age and $\delta^{18}O$ values, but have less extreme low-$\delta^{18}O$ obsidian values of ~ 3–4‰ (Bindeman and Valley 2001). The more voluminous later CPM rhyolites have low-$\delta^{18}O$ melt values of ~ 3–4‰ that match those of the early CPM units, but they possess less phenocrystic $\delta^{18}O$ heterogeneity than early CPM units (Bindeman and Valley 2001; Bindeman et al. 2008). U–Pb and U–Th zircon ages of later CPM rhyolites closely approximate their respective Ar–Ar eruption ages, and individual units reveal no or subtle zircon inheritance from pre-caldera source rocks (Vazquez and Reid 2002), with the possible exception of the voluminous Solfatara Plateau flow, which exhibits $\delta^{18}O$ zircon disequilibria (Bindeman et al. 2008) and possesses a Pb isotopic composition similar to that of HRT rocks (Vazquez et al. 2009).

Oxygen isotope insights into Yellowstone rhyolite petrogenesis

The high-latitude, high-altitude, intracontinental position of the Yellowstone caldera makes it possible to resolve meteoric water signatures in the oxygen isotopic compositions of erupted rhyolites. While it has long been recognized that large volumes of rhyolite produced by the Yellowstone caldera have drastic depletions in ^{18}O that require significant involvement of meteoric water (Friedman et al. 1974; Hildreth et al. 1984; Taylor 1986; Hildreth et al. 1991), the processes by which such depletions occurred were unclear until age and oxygen isotopic investigation of Yellowstone rhyolites on the single crystal scale (Bindeman and Valley 2000, 2001; Bindeman et al. 2001). Earlier interpretations included direct influx of meteoric waters into silicic magmas (Hildreth et al. 1984) or assimilation of wall rocks altered by hydrothermal fluids (Hildreth et al. 1991). As addressed by Bindeman and Valley (2000, 2001), each of these scenarios is unrealistic based on heat and mass-balance constraints. For instance, even in an extreme case of assimilation, in which the host magma and bulk assimilant are mixed in equal parts, the bulk assimilant would have to possess an exceptionally low-$\delta^{18}O$ value (<−6‰) to produce the observed UBM melt $\delta^{18}O$ values of ~ 0–2‰. However, such ultra low-$\delta^{18}O$ rocks are rare at Yellowstone caldera. Isotopic mixing

models yield considerably higher estimates of $\sim -1‰$ for the average $\delta^{18}O$ composition of low-$\delta^{18}O$ Yellowstone source rocks (Watts et al. 2010).

Individual zircon crystals from early UBM rhyolites of the Yellowstone caldera contain unequivocal age and oxygen isotopic evidence for inheritance from specific volcanic protoliths, supporting a magma genesis model of wholesale remelting of hydrothermally altered intracaldera blocks (Bindeman et al. 2008). Unique low-$\delta^{18}O$ signatures indicate that UBM rhyolites were generated by spatially discrete episodes of remelting, which yielded independent parcels of variably ^{18}O-depleted melts (Bindeman et al. 2008). This study builds on these and other previous results by presenting new age and O isotope data obtained by ion microprobe for individual zircons and Pb isotope data obtained by laser ablation for individual sanidines, for the youngest erupted post-caldera rhyolites of the Yellowstone caldera, the CPM rhyolites. In addition, we report new isotopic and age data for the oldest known UBM rhyolite, the East Biscuit Basin flow. With the addition of these important new datasets, we are able to construct an integrated model of post-LCT rhyolite genesis.

Samples and methods

We report new data for four young large-volume CPM rhyolites, including three lava flows (Pitchstone Plateau, West Yellowstone, Elephant Back) and one explosive tuff (Tuff of Bluff Point), two older, small-volume CPM rhyolite lavas (North Biscuit Basin, South Biscuit Basin), and one newly defined unit that represents the earliest and most primitive UBM rhyolite, the East Biscuit Basin flow (Fig. 1). These units span the full eruptive age range of post-LCT rhyolites and have a broad spatial distribution within the Yellowstone caldera (Fig. 1). With the exception of the East Biscuit Basin flow, which is one of the few low-silica rhyolites at Yellowstone, all samples are high-silica rhyolites with ~ 5–20 vol% sanidine, quartz, clinopyroxene, orthopyroxene, Fe–Ti oxides and accessory phases (see Supplementary Material 1 for petrographic descriptions, Supplementary Material 2 for photomicrographs, and Supplementary Material 3 for whole-rock major and trace element geochemistry). Notably, only North Biscuit Basin, South Biscuit Basin, and East Biscuit Basin flows have plagioclase, and East Biscuit Basin lacks sanidine and quartz. Abundant glass reentrants, sieved plagioclase phenocrysts, and anhedral crystal clusters were observed in samples of South Biscuit Basin and East Biscuit Basin lavas, consistent with the descriptions of Girard and Stix (2009). Zircon phenocrysts commonly occur as isolated crystals in the groundmass glass or as inclusions within Fe–Ti oxide and pyroxene aggregates. Most zircon
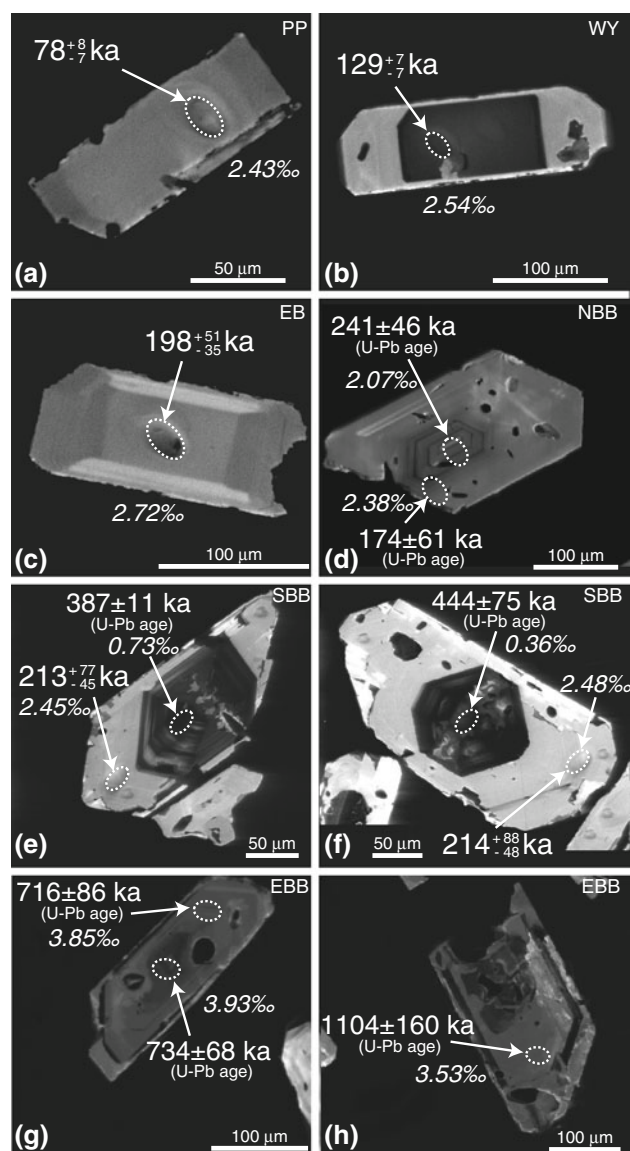

Fig. 2 Cathodoluminescence (CL) images of zircons dated for U-Th and U–Pb ages and analyzed for oxygen isotope compositions by ion microprobe. Analyzed spots are bounded by *dashed ellipses*. U-Th ages and uncertainties are shown in *bold text*; U–Pb ages are indicated by *parentheses*. Oxygen isotope compositions of dated zircon spots are shown in *italic text*. See Table 1 for a compilation of all ion microprobe data. **a** Pitchstone Plateau (PP) zircon, euhedral, and unzoned in CL. **b** West Yellowstone (WY) zircon, euhedral with distinct core-rim CL zoning. **c** Elephant Back (EB) zircon, euhedral with subtle core-rim CL zoning. **d** North Biscuit Basin (NBB) zircon exhibits core-rim zoning in CL, U–Pb age, and O isotope composition. **e, f** South Biscuit Basin (SBB) zircons, pronounced core-rim zoning in CL, U–Pb and U-Th age, and O isotope composition, cores are CL dark with subtle sector zoning. **g** East Biscuit Basin (EBB) zircon, zoned in CL and U–Pb age. **h** East Biscuit Basin (EBB) zircon has a U–Pb age that significantly predates the Lava Creek Tuff and post-Lava Creek Tuff eruptions

crystals are subhedral–euhedral, ~ 100–200 μm in length, and many exhibit cathodoluminescence (CL) zoning (Fig. 2).

U–Th disequilibrium dating of zircons was performed with a CAMECA ims 1270 ion microprobe at UCLA using a $\sim 30 \times 35$ μm spot size, according to the protocols described by Schmitt et al. (2006). Analytical details and operating conditions can be found in Supplementary Material 4. A small percentage (<10%) of the analyzed CPM zircon grains were found to be in ^{238}U–^{230}Th secular equilibrium and were reanalyzed for ^{238}U–^{206}Pb concordia ages according to the techniques outlined in Schmitt et al. (2003). Two Biscuit Basin samples (East Biscuit Basin and North Biscuit Basin) were dated for U–Pb ages at Stanford University using a SHRIMP-RG ion microprobe. For these analyses, the analytical techniques and conditions of Barth and Wooden (2010) were used.

All zircons dated for U–Th and U–Pb ages were analyzed for δ^{18}O compositions in subsequent analytical sessions at the UCLA SIMS facility. Back-scattered electron and CL images of zircon grain mounts enabled us to target the dated ion probe spots. After repolishing our zircon mounts according to the protocols of Kita et al. (2009), we determined the δ^{18}O compositions of the dated zircon spots a few microns below the original ion probe pits. Corrections for instrumental mass fractionation (IMF) were made using zircon standard KIM-5 (Valley 2003), mounted in the center of each zircon grain mount. KIM-5 zircons were analyzed repeatedly during each analytical session, with external errors that were typically less than 0.22‰ (1 SD) for each sample block (15–20 analyzed spots per block).

Pb isotope analyses of sanidine phenocrysts and host groundmass glasses were performed with a Finnigan Neptune MC-ICP-MS laser ablation system at Washington State University using the techniques and operating conditions of Kent (2008), as described in Supplementary Material 4. We analyzed four post-LCT units, including an older CPM rhyolite (South Biscuit Basin) and three younger CPM rhyolites (Pitchstone Plateau, Elephant Back, and the Tuff of Bluff Point), all of which were dated for U–Th and U–Pb ages and analyzed for δ^{18}O compositions by us. In addition, we measured Pb isotope ratios for sanidine separates from several members of major caldera-forming tuff eruptions at Yellowstone (HRT [members B and C] and LCT [member A]), which were previously studied for U–Pb ages and δ^{18}O compositions (Bindeman and Valley 2001; Bindeman et al. 2001, 2008).

Results

Results presented below include zircon crystallization ages and δ^{18}O compositions, and sanidine Pb isotope compositions. We also include whole-rock thermometry for all studied rhyolites and synthesize these new data with thermometry results from previous studies. The results in each

subsection are organized according to eruption age (oldest to youngest).

Zircon crystallization ages and δ^{18}O compositions

### Earliest Upper Basin Member rhyolite

Zircon dating of the most primitive rhyolite to erupt within the Yellowstone caldera, the East Biscuit Basin flow, indicates that it is also the oldest, with an error-weighted mean U–Pb age (781 ± 76 ka, $n = 9$, mean square of weighted deviates (MSWD) = 1.0). This age falls between the Ar–Ar eruption ages of the MFT and LCT (Fig. 3). No sanidine is present in the East Biscuit Basin flow, and our attempts to perform ^{40}Ar/^{39}Ar dating on plagioclase were unsuccessful, so we are unable to report an Ar–Ar eruption age for this unit. However, eruption of the East Biscuit Basin flow within the Yellowstone caldera near the Mallard Lake Resurgent dome (Fig. 1) indicates that it is a post-LCT rather than pre-LCT flow. The U–Pb zircon age range published by Bindeman et al. (2001) for the Middle Biscuit Basin flow overlaps the broad age range that we find for the East Biscuit Basin flow, and isotopically, the two units are similar (this study, Pritchard and Larson in review), suggesting that East Biscuit Basin and Middle Biscuit Basin flows may be related UBM units. Some East Biscuit Basin zircons are zoned in CL and U–Pb age (Fig. 2g), and the oldest zircons are generally present as fragments rather than whole grains (Table 1).

Complementary oxygen isotope data for dated East Biscuit Basin zircon spots reveal that it has zircon δ^{18}O values that are for the most part higher than LCT zircons, in contrast to other analyzed post-LCT units, which typically have lower zircon δ^{18}O values (c.f., Bindeman et al. 2008). However, East Biscuit Basin does have host glass and plagioclase with low-δ^{18}O values that are distinctive of post-LCT UBM units, 1.0 and 1.4‰, respectively. The average zircon δ^{18}O value of 4.3 ± 0.3‰ is more than 5‰ higher than the calculated equilibrium zircon value for East Biscuit Basin glass (Fig. 4) and is therefore one of the most extreme cases of oxygen isotopic disequilibrium documented for Yellowstone rhyolites. Unlike other UBM units, there is no clear core-rim δ^{18}O zoning in East Biscuit Basin zircons, and the δ^{18}O range of zircon cores and rims is relatively narrow ($\sim$2‰) compared to the exceptionally large ($\sim$6–8‰) range found for zircons from the Middle Biscuit Basin flow, Dunraven Road flow, and Canyon flow (Bindeman et al. 2008).

Early Central Plateau Member rhyolites

Zircon age data for the North Biscuit Basin and South Biscuit Basin flows corroborate earlier interpretations that

Fig. 3 U-Th and U–Pb ages of
individual Yellowstone zircons
determined by ion microprobe
(see Table 1 for data). *Left
panels* show error-weighted
probability distribution curves
for zircon analyses. U-Th zircon
ages are shown by the *light
bars*; zircons in or close to U-Th
secular equilibrium were dated
for U–Pb ages, shown by the
dark bars. Ar–Ar eruption ages
are shown by *thin vertical lines*
(Gansecki et al. 1996; Lanphere
et al. 2002; Christiansen et al.
2007, this study). The K–Ar
eruption age for the Elephant
Back flow is from Obradovich
(1992). For the Pitchstone
Plateau flow and West
Yellowstone flow, we include
the mean U-Th ages (*thin
dashed lines*) and error fields
(*shaded*) published by Vazquez
and Reid (2002) for these units.
Right panels show individual
zircon analyses (light squares
for U-Th ages and dark squares
for U–Pb ages) are shown with
their error bars (±1σ). *Bold
vertical lines* show the error-
weighted mean U-Th and U–Pb
zircon ages. *Thin vertical lines*
show the eruption ages (as
indicated and labeled in the *left
panels*)
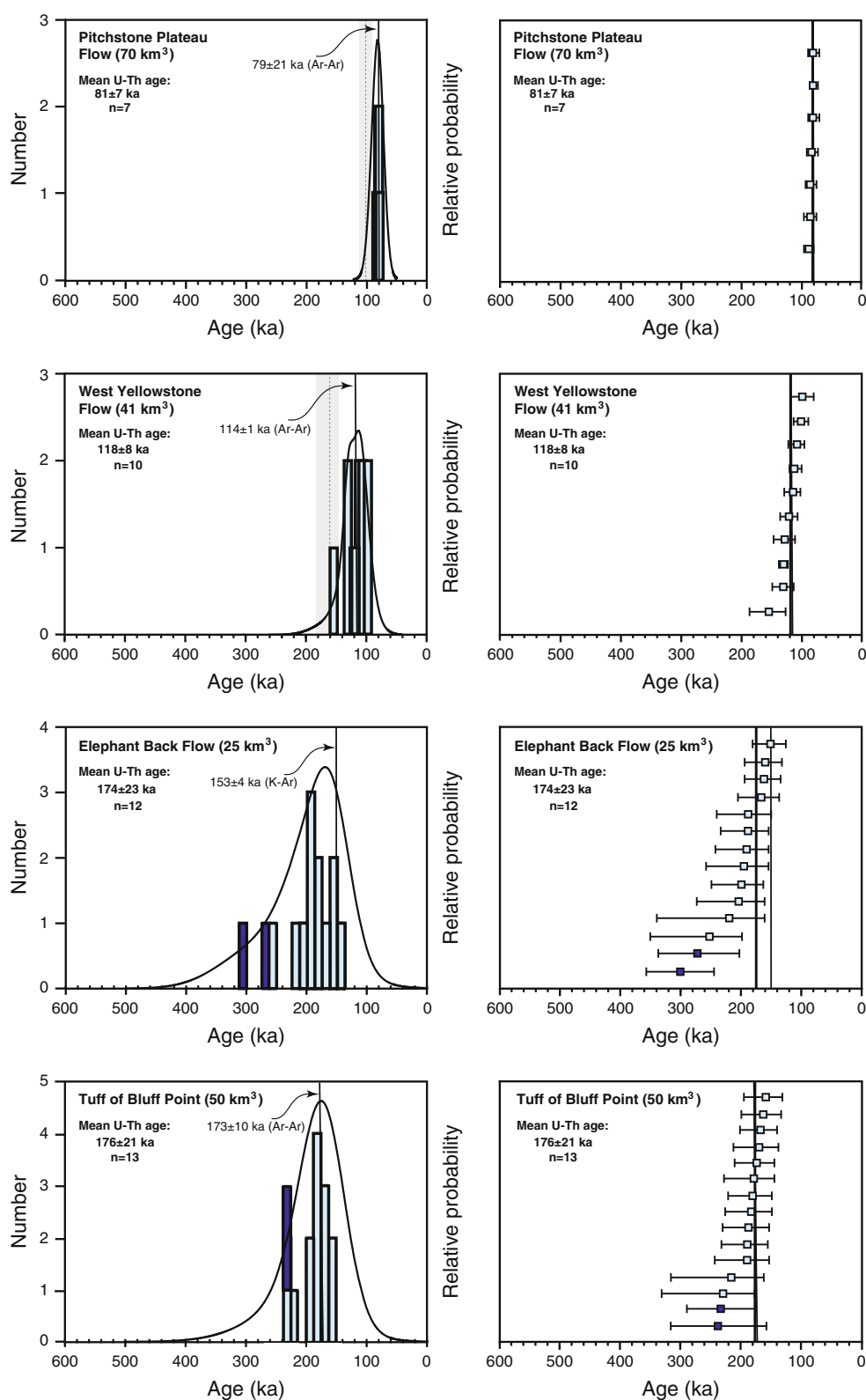
they are distinct units rather than a single Biscuit Basin
rhyolite (Bindeman et al. 2008). The North Biscuit Basin
flow has an error-weighted mean U–Pb age (190 ± 45 ka,
n = 9, MSWD = 0.4) that is unimodal and normally

distributed (Fig. 3), consistent with our findings for CPM
rhyolites (see next section). The ⁴⁰Ar/³⁹Ar sanidine erup-
tion age determined by us for North Biscuit Basin
(155 ± 9 ka) is within the 170–75 ka age range of CPM

Fig. 3 continued
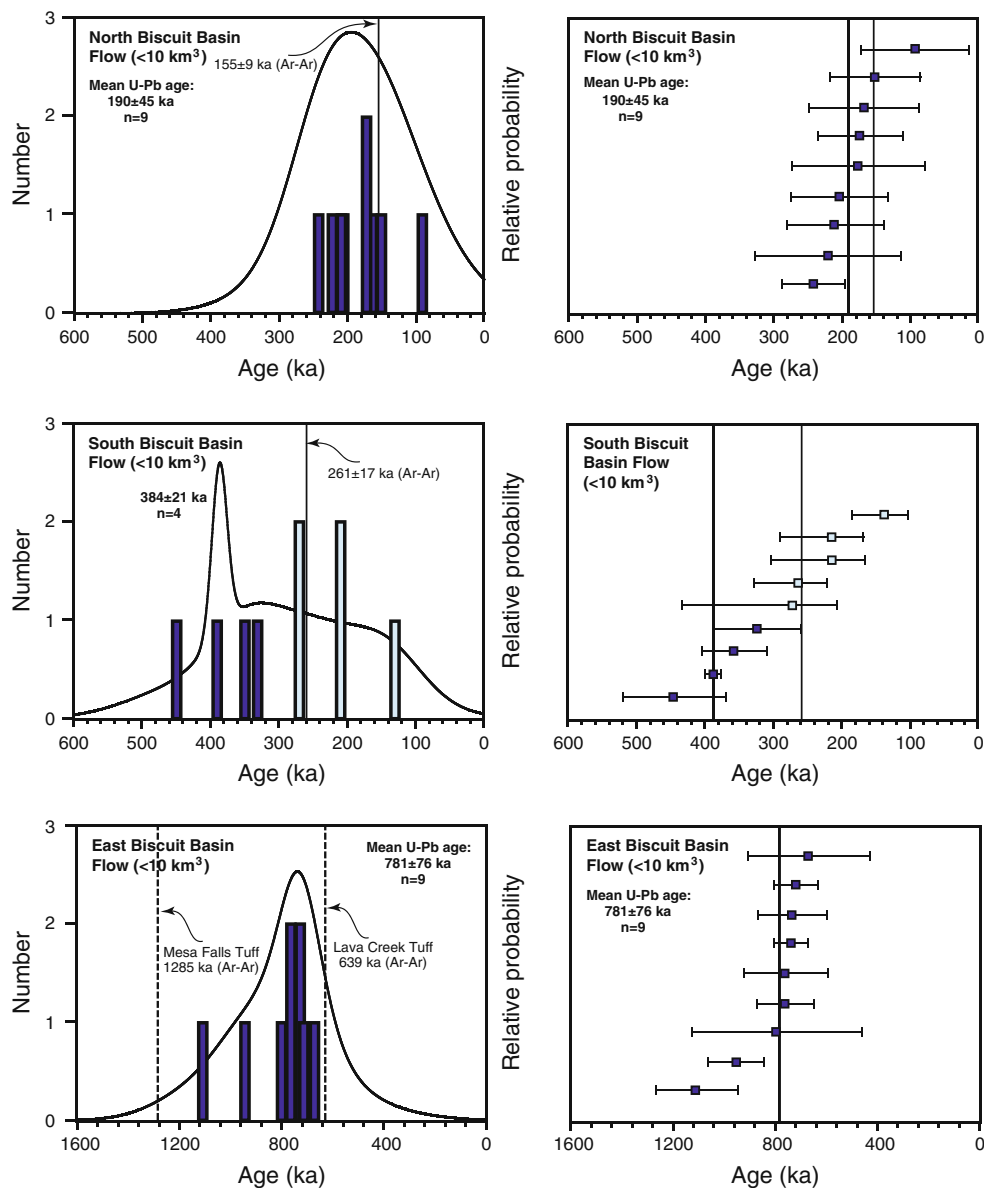
rhyolite eruptions (Christiansen et al. 2007), indicating that it is an early CPM unit. Core-rim zoning of North Biscuit Basin zircons is apparent in CL and U–Pb age (Fig. 2d), with the oldest core ages closely approximating the Ar–Ar eruption age of the oldest CPM unit, the Scaup Lake flow (257 ± 13 ka; Christiansen et al. 2007).

South Biscuit Basin flow has a non-normally distributed zircon age population that spans a broad age range (Fig. 3). The error-weighted mean U–Pb age of the oldest South Biscuit Basin age peak (384 ± 21 ka, $n = 4$, MSWD = 0.7) significantly predates the onset of CPM eruptions (∼260 ka). South Biscuit Basin zircons exhibit distinct core-rim zoning in both CL and age (Fig. 2e, f). U–Th ages of zircon rims typically overlap the $^{40}Ar/^{39}Ar$ sanidine eruption age within error (261 ± 17 ka; Fig. 3). This evidence suggests that the South Biscuit Basin flow contains

antecrystic zircon crystals, with cores that skew the apparent U–Pb age to older values, and overgrowth rims that reflect younger zircon growth prior to eruption.

Like the zircon age data, oxygen isotope data for dated zircon spots require that the North Biscuit Basin and South Biscuit Basin flows be treated as separate Biscuit Basin units (Fig. 4). North Biscuit Basin has an average zircon $\delta^{18}O$ value of 2.7 ± 0.2‰, which is identical to the average zircon $\delta^{18}O$ values determined for the CPM Tuff of Bluff Point and Elephant Back flow (see next section). North Biscuit Basin zircon rims fall within the same $\delta^{18}O$ range as zircon cores, and there is no discernable core-rim zoning; however, the calculated equilibrium zircon $\delta^{18}O$ value with host glass is about 0.5‰ lower than the average zircon value, indicating subtle oxygen isotopic disequilibrium. South Biscuit Basin exhibits more extreme $\delta^{18}O$

Table 1 U-Th and U–Pb ages, δ^{18}O values, and sizes of zircons in studied Yellowstone rhyolites

Sample	Core-rim	Model U-Th age (ka)[a]	+1σ	−1σ	U–Pb concordia age (ka)	±1σ	δ^{18}O (‰) (same spot)	δ^{18}O (‰) (adjacent)	±1σ ext	Length (μm)	Width (μm)
Pitchstone Plateau flow (YL02-1)											
YL02-1_g1	C	83	9	−9	–	–	3.16	3.02	0.22	133	77
YL02-1_g2	C	82	10	−9	–	–	3.01	3.23	0.22	117	51
YL02-1_g3	C	78	8	−7	–	–	2.43	–	0.22	144	54
YL02-1_g5	C	84	11	−10	–	–	2.61	3.01	0.22	218	60
YL02-1_g6	C	87	9	−8	–	–	2.44	2.61	0.22	108	56
YL02-1_g7	C	78	10	−9	–	–	2.85	–	0.22	82	49
YL02-1_g8	C	79	9	−9	–	–	2.14	2.90	0.22	104	61
West Yellowstone flow (YL96-1)											
YL96-1_g1	C	129	7	−7	–	–	2.54	3.08	0.22	231	73
YL96-1_g2	C	126	19	−16	–	–	2.92	2.85	0.22	175	104
YL96-1_g3	C	153	34	−26	–	–	2.94	2.67	0.22	243	110
YL96-1_g4	C	98	21	−17	–	–	2.38	2.41	0.22	188	103
YL96-1_g5	C	120	15	−13	–	–	3.08	–	0.22	154	66
YL96-1_g6	C	110	10	−9	–	–	2.95	–	0.22	204	83
YL96-1_g7	C	100	13	−12	–	–	2.69	3.18	0.22	203	90
YL96-1_g8	C	114	15	−13	–	–	2.58	2.72	0.22	189	75
YL96-1_g9	C	129	20	−17	–	–	3.11	3.04	0.22	169	79
YL96-1_g10	C	107	14	−13	–	–	2.90	–	0.22	178	72
Elephant Back flow (06YS-4)											
YS-4_g1	C	345	∞	−124	271	67	3.26	–	0.22	219	104
YS-4_g2	C	187	54	−36	–	–	3.57	–	0.22	216	84
YS-4_g3	C	189	54	−36	–	–	2.87	2.51	0.22	197	77
YS-4_g4	C	198	51	−35	–	–	2.72	3.21	0.22	179	79
YS-4_g5	C	149	32	−24	–	–	2.64	–	0.22	220	86
YS-4_g6	C	250	101	−52	300	56	2.83	2.52	0.22	245	94
YS-4_g8	C	194	65	−40	–	–	2.48	–	0.22	207	97
YS-4_g9	C	165	40	−29	–	–	2.40	3.21	0.22	160	74
YS-4_g10	C	187	48	−33	–	–	2.42	–	0.22	186	71
YS-4_g11	C	203	71	−43	–	–	3.07	–	0.22	248	82
YS-4_g12	C	218	123	−56	–	–	2.34	–	0.22	153	89
YS-4_g13	C	160	36	−27	–	–	2.59	2.51	0.22	131	60
YS-4_g14	C	160	34	−26	–	–	2.15	–	0.22	304	114
Tuff of Bluff Point (06YS-2)											
YS-2_g1	C	368	∞	−132	237	79	2.36	2.60	0.22	371	142
YS-2_g2	C	189	54	−36	–	–	2.74	2.86	0.22	256	91
YS-2_g3	C	170	44	−31	–	–	2.89	2.84	0.22	300	112
YS-2_g4	C	159	37	−28	–	–	2.67	2.70	0.22	338	131
YS-2_g5	C	179	50	−34	–	–	2.84	2.49	0.22	397	119
YS-2_g6	C	188	44	−31	–	–	2.94	2.52	0.22	263	107
YS-2_g7	C	173	39	−28	–	–	2.90	2.74	0.22	182	108
YS-2_g8	C	186	45	−32	–	–	2.65	2.29	0.22	277	120
YS-2_g9	C	167	35	−26	–	–	2.85	2.87	0.22	272	90
YS-2_g10	C	162	37	−28	–	–	2.25	2.30	0.22	245	106
YS-2_g11	C	229	103	−52	232	57	2.98	2.72	0.22	276	111
YS-2_g12	C	180	42	−30	–	–	2.56	2.44	0.22	247	118
YS-2_g13	C	215	102	−52	–	–	2.60	3.09	0.22	203	102
YS-2_g14	C	182	45	−32	–	–	2.39	2.73	0.22	237	140

Table 1 continued

Sample	Core-rim	Model U-Th age (ka)[a]	+1σ	−1σ	U–Pb concordia age (ka)	±1σ	δ18O (‰) (same spot)	δ18O (‰) (adjacent)	±1σ ext	Length (μm)	Width (μm)
North Biscuit Basin flow (08YS-14)											
KWBBRR-2.1	C	–	–	–	92	79	3.22	3.22	0.35	357	214
KWBBR-4.1	C	–	–	–	151	66	2.71	6.74	0.35	Fragment	Fragment
KWBBR-3.1	C	–	–	–	168	80	2.61	2.71	0.35	Fragment	Fragment
KWBBR-8.1	R	–	–	–	175	97	2.82	2.52	0.35	276	149
KWBBRR-9.1	R	–	–	–	174	61	2.38	–	0.35	–	–
KWBBR-7.1	C	–	–	–	204	71	2.70	2.74	0.35	229	85
KWBBR-2.1	C	–	–	–	210	72	2.90	–	0.35	328	162
KWBBR-5.1	R	–	–	–	221	106	3.29	2.30	0.35	Fragment	Fragment
KWBBRC-9.2	C	–	–	–	241	46	2.07	–	0.35	288	114
South Biscuit Basin flow (YL96-2)											
YL2_58-3	R	213	77	−45	–	–	2.45	–	0.20	–	–
YL2_52-1	C	137	50	−34	–	–	−0.20	–	0.20	300	105
YL2_5-2	R	262	65	−40	–	–	2.13	–	0.24	–	–
YL2_52-3	R	270	164	−63	–	–	2.39	–	0.20	–	–
YL2_59-2	R	214	88	−48	–	–	2.48	–	0.24	–	–
YL2_6-2	R	356	∞	−134	322	64	2.37	–	0.24	–	–
YL2_58-1	C	321	306	−72	387	11	0.73	–	0.20	260	110
YL2_59-1	C	449	∞	−123	444	75	0.36	–	0.24	300	140
YL2_6-1	C	326	∞	−103	357	46	1.55	–	0.24	215	70
East Biscuit Basin flow (08YS-15b)											
KWEBB-2.1	C	–	–	–	667	236	5.13	4.90	0.35	135	144
KWEBB-9.1	R	–	–	–	716	86	3.85	4.07	0.35	–	–
KWEBB-8.1	C	–	–	–	734	68	3.93	–	0.35	257	89
KWEBB-6.1	C	–	–	–	733	137	4.05	–	0.35	204	86
KWEBB-4.1	R	–	–	–	757	166	3.90	4.41	0.35	220	129
KWEBB-7.1	C	–	–	–	761	110	4.84	4.99	0.35	Fragment	Fragment
KWEBB-1.1	C	–	–	–	793	334	3.98	–	0.35	Fragment	Fragment
KWEBB-3.1	C	–	–	–	949	111	4.94	–	0.35	Fragment	Fragment
KWEBB-5.1	C	–	–	–	1,104	160	3.53	3.63	0.35	Fragment	Fragment

[a] Model ages were calculated using zircon–vitrophyre isochrons. Published thermal ionization mass spectrometry (TIMS) data for U and Th isotopes of CPM vitrophyres (Vazquez and Reid 2002) were used to estimate the initial ^{230}Th abundances of CPM zircons; average activity ratios of (^{230}Th)/(^{232}Th) = 0.78 ± 0.05 and (^{238}U)/(^{232}Th) = 0.72 ± 0.05 were used for CPM units without published TIMS data. Decay constants: λ_{230}: 9.158 × 10^{-6} year^{-1}; λ_{232}: 4.9475 × 10^{-11} year^{-1}; λ_{238}: 1.55125 × 10^{-10} year^{-1}

disequilibrium, with zircons that are up to 2‰ lower than the equilibrium value, though zircon rims more closely approximate an equilibrium value (Fig. 4). The calculated equilibrium zircon δ^{18}O value for South Biscuit Basin is about 1‰ lower than equilibrium values for other CPM units, but clearly more similar in oxygen isotopic composition to CPM than to UBM rhyolites.

Later Central Plateau Member rhyolites

Zircon ages for studied CPM rhyolite samples are unimodal and do not exhibit xenocrystic or antecrystic age inheritance (Fig. 3), in contrast to the significant zircon age

heterogeneity documented for UBM samples (Bindeman et al. 2001). Error-weighted mean U–Th ages for the Pitchstone Plateau flow (81 ± 7 ka, $n = 7$, MSWD = 0.2), West Yellowstone flow (118 ± 8 ka, $n = 10$, MSWD = 1.1), and Tuff of Bluff Point (176 ± 21 ka, $n = 13$, MSWD = 0.1) are identical to ^{40}Ar/^{39}Ar sanidine eruption ages published by Christiansen et al. (2007) for these units (Fig. 3). Mean U–Th zircon ages previously reported by Vazquez and Reid (2002) for the Pitchstone Plateau and West Yellowstone flows (dashed lines and shaded error fields in Fig. 3) are slightly older than our mean U–Th age estimates, owing to the fact that these authors found and included some antecrysts in their age averages,
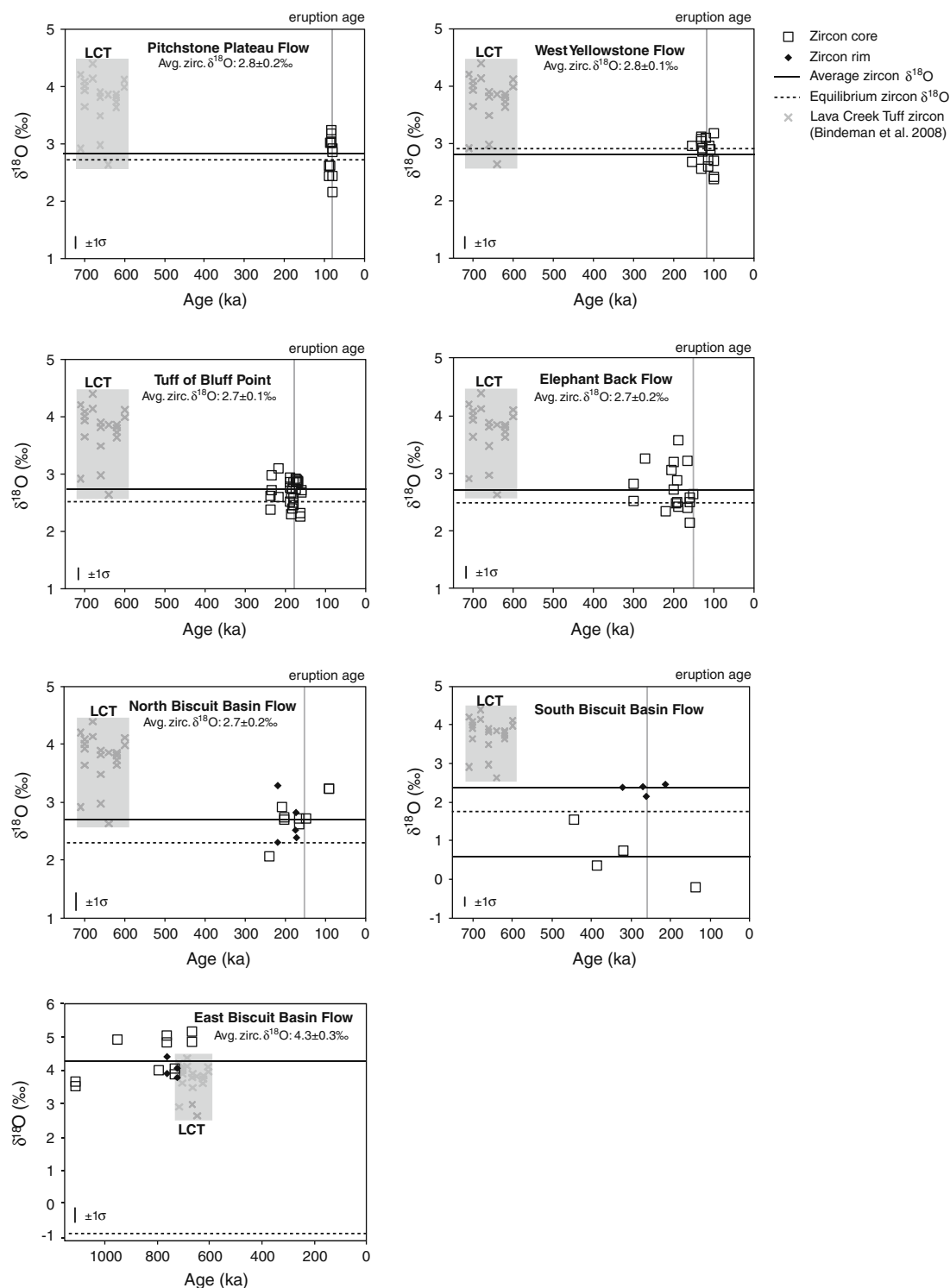
Fig. 4 Oxygen isotope compositions of individual Yellowstone zircons determined by ion microprobe (see Table 1 for data). Oxygen isotope compositions are plotted against U-Th and U–Pb ages for individual zircon spots. Average zircon $\delta^{18}O$ values for each unit are shown by the *solid horizontal lines*. For the South Biscuit Basin flow, we include two average zircon $\delta^{18}O$ values (zircon cores and their rims). Equilibrium zircon $\delta^{18}O$ values, calculated using host glass $\delta^{18}O$ values and $\Delta^{18}O_{\text{melt-zircon}} = 1.9‰$ (applicable for liquidus temperatures of $\sim 800°C$; Bindeman and Valley 2002), are shown by the *dashed horizontal lines*. For reference, we include the age and oxygen isotope field for Lava Creek Tuff (LCT) zircons (*shaded* Bindeman et al. 2008) and eruption ages of the studied post-caldera rhyolites (*vertical gray lines* see Fig. 4 for references). Uncertainties (1σ) for individual zircon $\delta^{18}O$ measurements are shown in the *bottom left corner* of *each panel*

whereas no antecrysts were apparent by our analyses. The error-weighted mean U–Th age for the Elephant Back flow (174 ± 23 ka, $n = 12$, MSWD = 0.3) is 21 ky older than this unit's published K–Ar sanidine eruption age (Obradovich 1992) (Fig. 3). A few older zircon crystals in the Elephant Back flow and the Tuff of Bluff Point were found to be in ^{238}U–^{230}Th secular equilibrium and redated with U–Pb (dark bars in Fig. 3). However, these older zircon grains are within uncertainty of the U–Th zircon age dating methods. Vazquez and Reid (2002) reported the presence of older zircon grains in several CPM units (Pitchstone Plateau flow, Solfatara Plateau flow, West Yellowstone flow, and Dry Creek flow) that match the ~ 250–300 ka ages of the older grains that we find for the Elephant Back flow and Tuff of Bluff Point.

Oxygen isotope ratios determined by ion microprobe for dated CPM zircon spots generally overlap within uncertainty (Table 1) and are about 1‰ depleted relative to LCT zircons (Fig. 4). Pitchstone Plateau flow and West Yellowstone flow have identical average zircon $\delta^{18}O$ values of 2.8 ± 0.2 and 2.8 ± 0.1‰, respectively, which closely approximate the calculated equilibrium zircon $\delta^{18}O$ values based on laser-fluorination data for host glass and major phenocryst phases of quartz and sanidine. The Tuff of Bluff Point and Elephant Back flow have slightly lower, but overlapping, average zircon $\delta^{18}O$ values of 2.7 ± 0.1 and 2.7 ± 0.2‰, respectively (Fig. 4). Calculated equilibrium zircon $\delta^{18}O$ values for the Tuff of Bluff Point and Elephant Back flow are about 0.25‰ lower than the average zircon $\delta^{18}O$ values obtained by ion microprobe, but overlap the equilibrium estimates within error (Fig. 4).

Comparison of oxygen isotope data for all studied Yellowstone rhyolites

When our new zircon data are combined with all published ion microprobe oxygen isotope data for Yellowstone rhyolites (Fig. 5a, arrows indicate the new units presented in this study), the following features are apparent: (1) East Biscuit Basin flow has zircons with oxygen isotope values that are generally higher than other post-LCT units, but has a low-$\delta^{18}O$ glass value that is distinctive of UBM lavas, (2) North Biscuit Basin zircons fall within the oxygen isotope range defined by CPM lavas, (3) CPM rhyolites have zircons with more homogeneous oxygen isotope compositions than older Yellowstone rhyolites, (4) CPM zircons generally have oxygen isotopic compositions that are in equilibrium with coexisting phenocrysts and groundmass glasses, and (5) zircon compositions of individual CPM units overlap within a relatively narrow $\delta^{18}O$ range. Taken together, this new evidence indicates that CPM rhyolites can be distinguished from older Yellowstone rhyolites by

their relatively homogeneous low-$\delta^{18}O$ zircon oxygen isotope compositions that are in equilibrium with host melts, whereas UBM rhyolites are more complex, retaining significant zircon oxygen isotope heterogeneity and disequilibria in low-$\delta^{18}O$ melts. In addition to a trend of increasing homogeneity through time (Fig. 5a), we also observe a positive correlation between zircon homogeneity and eruptive volume, in which more voluminous post-caldera rhyolites tend to have narrower zircon $\delta^{18}O$ ranges (Fig. 5b).

Lead isotope compositions of individual sanidines

Major caldera-forming tuffs

Lead isotope compositions measured for individual sanidine crystals from HRT and LCT rocks define separate arrays that can be used to differentiate individual units (Fig. 6a). Similar results were obtained for groundmass glasses of HRT, MFT, and LCT, in which case Pb isotopes can be used to distinguish different compositional fields of tuff members (Doe et al. 1982; Hildreth et al. 1991, light gray ellipses in Fig. 6a). Our new Pb isotope data for individual sanidines show that these isotopic differences also exist on the crystal scale, and we find that sanidines from two different members of the first major caldera-forming eruption at Yellowstone, HRT members B and C, bracket the entire range of Yellowstone rhyolite Pb isotope compositions (Fig. 6a). HRT member C has a bimodal Pb isotope composition, with one population that possesses an exceptionally radiogenic Pb isotope signature, while HRT member B has the least radiogenic Pb isotope signature of the units analyzed in this study, falling within the compositional field of Yellowstone basalts (dark gray field in Fig. 6a). In addition, HRT member B has more homogeneous sanidine Pb isotope compositions than HRT member C or LCT member A (Fig. 6a), perhaps indicating less crustal contamination in HRT member B relative to other tuff members.

Central Plateau Member rhyolites

The isotopic array defined by CPM sanidines is distinct from those of the caldera-forming tuffs that predate them (Fig. 6a). The fact that the CPM sanidine field does not intersect the LCT field (Fig. 6a) indicates that CPM rhyolites cannot be magmatic remnants of the LCT batholith, in contrast to the early interpretations of Hildreth et al. (1984). We observe that CPM lead isotope ratios fall between the HRT and LCT fields (Fig. 6a), consistent with the interpretations of Bindeman et al. (2008) for derivation of post-LCT rhyolites from
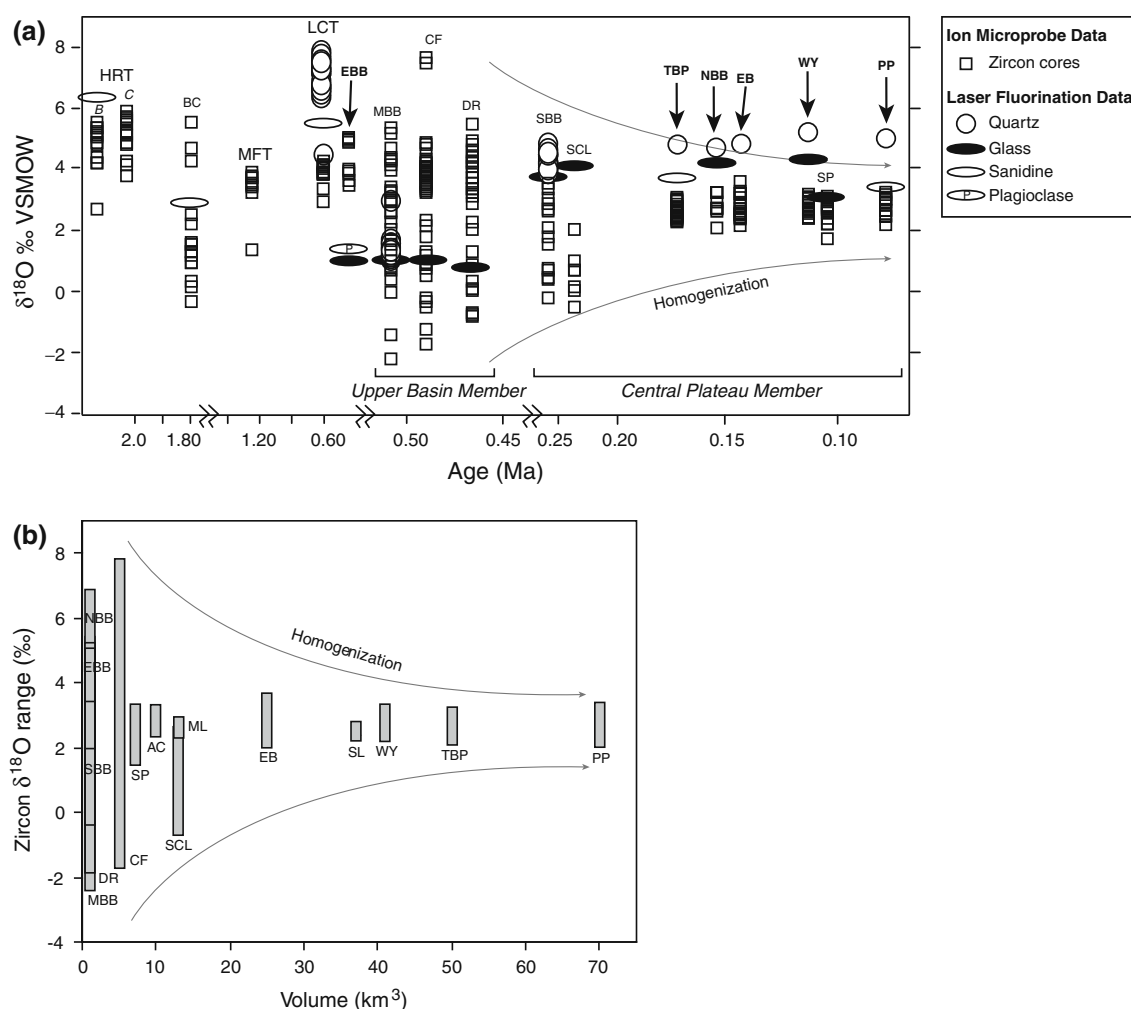
Fig. 5 a Ion microprobe analyses of $\delta^{18}O$ in zircon (*squares*) plotted against eruption ages for Yellowstone rhyolites. Laser-fluorination $\delta^{18}O$ data for quartz (*circles*), sanidine (*open ovals*), and glass (*filled ovals*) are also included. Our new oxygen isotope data for six post-Lava Creek Tuff units (denoted by *arrows*) are synthesized with data published by Bindeman et al. (2008). Our new data reveal a trend of increasing homogenization of zircon $\delta^{18}O$ compositions with decreasing eruption age (trend shown with *light gray arrows*). Unit abbreviations are as follows: Huckleberry Ridge Tuff (HRT) members B and C; Blue Creek flow (BC); Mesa Falls Tuff (MFT); Lava Creek Tuff (LCT); East Biscuit Basin flow (EBB); Middle Biscuit Basin flow (MBB); Canyon flow (CF); Dunraven Road flow (DR); South Biscuit Basin flow (SBB); Scaup Lake flow (SCL); Tuff of Bluff Point (TBP); North Biscuit Basin flow (NBB); Elephant Back flow (EB); West Yellowstone flow (WY); Solfatara Plateau flow (SP);

Pitchstone Plateau flow (PP). Eruption ages are from Obradovich (1992), Gansecki et al. (1996), Lanphere et al. (2002), Christiansen et al. (2007), Bindeman et al. (2008), and this study. No eruption age is available for the post-LCT EBB flow; it is plotted immediately after LCT. Symbols for SBB and SCL, and NBB and EB were slightly offset from one another to avoid overlap. Modified after Bindeman et al. (2008). **b** Zircon $\delta^{18}O$ ranges plotted against eruptive volumes for post-Lava Creek Tuff rhyolites. Zircon $\delta^{18}O$ ranges are from Bindeman and Valley (2001), Bindeman et al. (2008) and this study. Eruptive volumes are from Christiansen et al. (2007). Our new data reveal a trend of increasing homogenization of zircon $\delta^{18}O$ compositions with increasing eruptive volume (trend shown with light gray arrows). Unit abbreviations are the same as those used in **a**, with the addition of post-Lava Creek Tuff units Aster Creek flow (AC), Mallard Lake flow (ML), and Summit Lake flow (SL)

remelting of HRT, LCT, and pre-LCT intracaldera rocks; however, we note that other isotopic parameters necessitate contribution from additional sources, and therefore, it is not possible to derive post-LCT rhyolites through simple binary mixing of these two end members (see next section). Similar to the results for Pb isotope compositions of CPM groundmass glasses (Doe et al. 1982; Vazquez et al. 2009, light gray ellipses in Fig. 6a, b), the

CPM sanidines analyzed in this study have overlapping Pb isotope compositions that define a unique array. Glass analyses from our rhyolite mounts (open symbols) fall within the Pb isotope fields defined by the sanidines (filled symbols) for each CPM rhyolite (Fig. 6b). One notable outlier of the CPM group is the Solfatara Plateau flow ("SP" in Fig. 6a), which has a glass composition that falls outside of the defined CPM lead isotope field
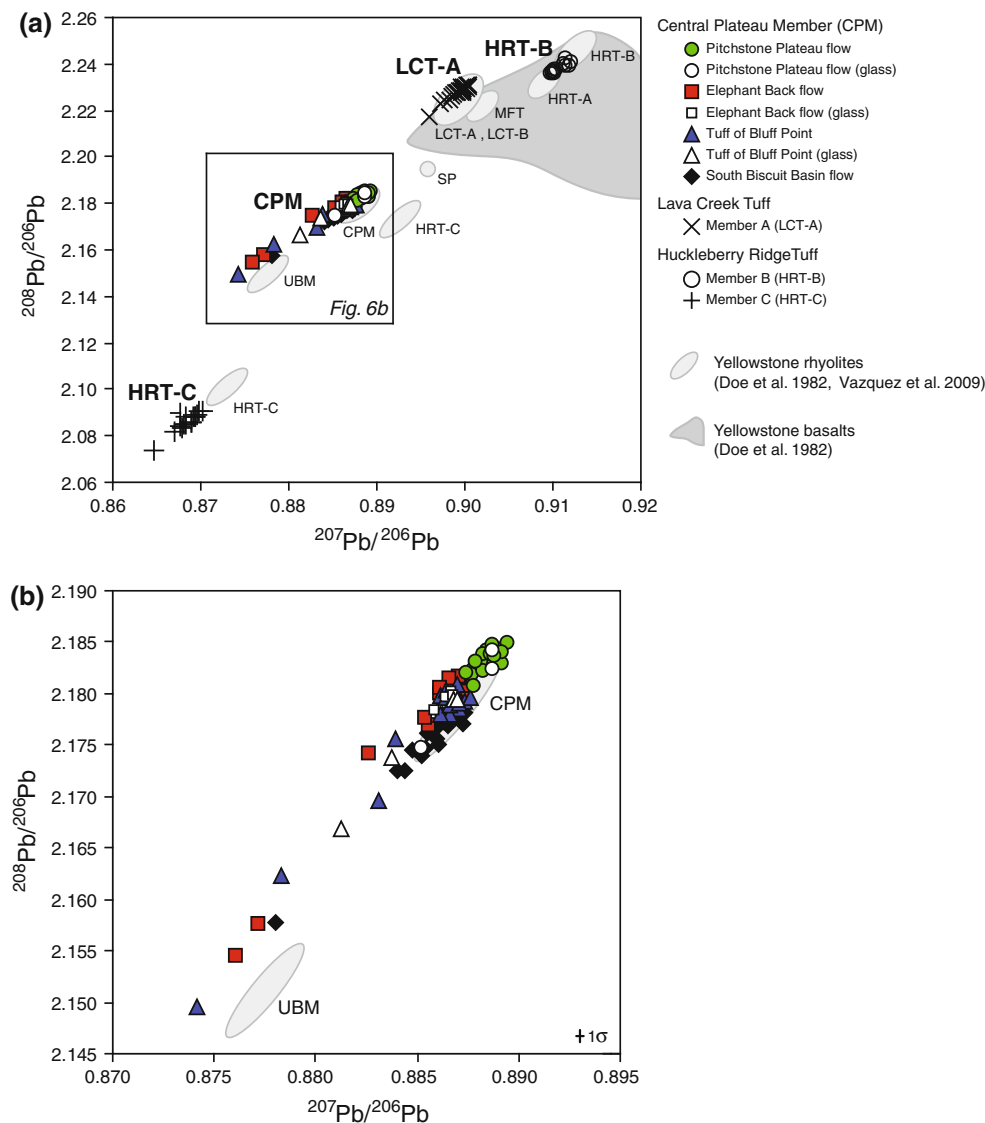
Fig. 6 a Lead isotope compositions of individual Yellowstone sanidines determined by laser ablation (see Table 2 for data) and published whole-rock and glass compositions of Yellowstone rhyolites (*gray ellipses*) and basalts (*dark gray field*). Host glass analyses for the Central Plateau Member (CPM) rhyolites analyzed in this study are shown by the *open symbols*. Distinct lead isotope compositions are apparent for Huckleberry Ridge Tuff members B and C (HRT-B and HRT-C), Lava Creek Tuff member A (LCT-A), and CPM rhyolites. Note that post-LCT CPM rhyolites do not overlap the LCT compositional array and therefore cannot be remnants of LCT magma that remained after caldera collapse. Abbreviations for Yellowstone units from Doe et al. (1982) and Vazquez et al. (2009)

are as follows: Huckleberry Ridge Tuff member A (HRT-A), Mesa Falls Tuff (MFT), Lava Creek Tuff member B (LCT-B), Solfatara Plateau flow (SP), Upper Basin Member (UBM). **b** Higher resolution version of **a**, showing lead isotope variation within the CPM rhyolite group. Note that the Pitchstone Plateau flow sanidines and glasses (*filled* and *open circles*) form a distinct lead isotope end member in the CPM array and have more homogeneous lead isotope compositions than older CPM units. Older CPM units exhibit more heterogeneity and have lead isotopic compositions that are more similar to those for UBM rhyolites. The average external error (±1σ) for lead isotope analyses is shown in the *bottom right corner*

(Vazquez et al. 2009). We also observe that the Elephant Back flow, Tuff of Bluff Point, and South Biscuit Basin flow have heterogeneous sanidine compositions, some of which more closely approximate the Pb isotopic composition of the UBM rather than CPM array (Fig. 6b). In contrast, the Pitchstone Plateau flow sanidines are the most homogeneous and form a less radiogenic Pb isotopic end member (Fig. 6b).

Comparison with published radiogenic isotope datasets

It is apparent from published Sr, Nd, and Pb isotope datasets for CPM whole-rocks and glasses that multiple sources, including Yellowstone basalts and highly radiogenic Archean crust, must be accounted for in any realistic isotopic mixing models for Yellowstone rhyolites (Hildreth et al. 1991; Vazquez et al. 2009; Watts et al.

Table 2 Pb isotopes of sanidines in studied Yellowstone rhyolites

Sample	$^{206}Pb/^{204}Pb$	$\pm1\sigma$ ext	$^{207}Pb/^{204}Pb$	$\pm1\sigma$ ext	$^{208}Pb/^{204}Pb$	$\pm1\sigma$ ext	$^{207}Pb/^{206}Pb$	$\pm1\sigma$ ext	$^{208}Pb/^{206}Pb$	$\pm1\sigma$ ext
Pitchstone Plateau flow (YL02-1)										
YL02-1_1.1	13.37	0.32	11.89	0.29	29.07	0.72	0.8889	0.0006	2.1844	0.0009
YL02-1_1.2	13.02	0.32	11.58	0.29	28.33	0.72	0.8883	0.0006	2.1837	0.0009
YL02-1_1.3	13.46	0.32	11.96	0.29	29.25	0.72	0.8887	0.0006	2.1838	0.0009
YL02-1_1.4	13.51	0.32	11.99	0.29	29.36	0.72	0.8884	0.0006	2.1839	0.0009
YL02-1_2.1	14.27	0.32	12.67	0.29	31.02	0.72	0.8884	0.0006	2.1830	0.0009
YL02-1_2.2	14.07	0.32	12.50	0.29	30.62	0.72	0.8884	0.0006	2.1841	0.0009
YL02-1_2.3	14.24	0.32	12.66	0.29	30.99	0.72	0.8889	0.0006	2.1836	0.0009
YL02-1_4.1	11.88	0.32	10.52	0.29	25.76	0.72	0.8878	0.0006	2.1823	0.0009
YL02-1_4.2	12.62	0.32	11.20	0.29	27.39	0.72	0.8882	0.0006	2.1831	0.0009
YL02-1_4.3	12.28	0.32	10.91	0.29	26.68	0.72	0.8882	0.0006	2.1837	0.0009
YL02-1_5.1	12.13	0.32	10.77	0.29	26.30	0.72	0.8892	0.0006	2.1830	0.0009
YL02-1_5.2	8.24	0.32	7.31	0.29	17.69	0.72	0.8887	0.0006	2.1846	0.0009
YL02-1_5.3	11.75	0.32	10.41	0.29	25.47	0.72	0.8888	0.0006	2.1837	0.0009
YL02-1_6.1	11.37	0.32	10.09	0.29	24.60	0.72	0.8877	0.0006	2.1818	0.0009
YL02-1_6.2	11.83	0.32	10.50	0.29	25.63	0.72	0.8883	0.0006	2.1822	0.0009
YL02-1_6.3	11.74	0.32	10.43	0.29	25.43	0.72	0.8886	0.0006	2.1837	0.0009
YL02-1_7.1	10.97	0.32	9.72	0.29	23.78	0.72	0.8879	0.0006	2.1832	0.0009
YL02-1_7.2	11.61	0.32	10.29	0.29	25.15	0.72	0.8874	0.0006	2.1820	0.0009
YL02-1_7.3	12.55	0.32	11.13	0.29	27.21	0.72	0.8878	0.0006	2.1808	0.0009
YL02-1_8.1	12.48	0.32	11.07	0.29	27.09	0.72	0.8895	0.0006	2.1849	0.0009
YL02-1_8.2	12.55	0.32	11.14	0.29	27.23	0.72	0.8892	0.0006	2.1839	0.0009
YL02-1_8.3	12.77	0.32	11.34	0.29	27.72	0.72	0.8888	0.0006	2.1837	0.0009
YL02-1_glass-1	13.75	0.32	12.22	0.29	29.90	0.72	0.8887	0.0006	2.1823	0.0009
YL02-1_glass-2	12.48	0.32	11.04	0.29	26.99	0.72	0.8853	0.0006	2.1748	0.0009
YL02-1_glass-3	12.70	0.32	11.24	0.29	27.53	0.72	0.8887	0.0006	2.1841	0.0009
Elephant Back flow (06YS-4)										
06YS-4_2.1	11.28	0.18	9.88	0.16	24.13	0.38	0.8772	0.0004	2.1575	0.0012
06YS-4_2.2	11.52	0.18	10.20	0.16	24.93	0.38	0.8870	0.0004	2.1816	0.0012
06YS-4_2.3	11.65	0.18	10.20	0.16	24.93	0.38	0.8760	0.0004	2.1545	0.0012
06YS-4_2.4	11.40	0.18	10.08	0.16	24.63	0.38	0.8868	0.0004	2.1798	0.0012
06YS-4_3.1	8.79	0.18	7.75	0.16	18.86	0.38	0.8865	0.0004	2.1801	0.0012
06YS-4_3.2	8.16	0.18	7.18	0.16	17.46	0.38	0.8862	0.0004	2.1801	0.0012
06YS-4_3.3	10.43	0.18	9.22	0.16	22.49	0.38	0.8869	0.0004	2.1798	0.0012
06YS-4_4.1	11.08	0.18	9.79	0.16	23.91	0.38	0.8867	0.0004	2.1796	0.0012
06YS-4_4.2	11.82	0.18	10.47	0.16	25.56	0.38	0.8874	0.0004	2.1802	0.0012
06YS-4_4.3	12.59	0.18	11.15	0.16	27.25	0.38	0.8870	0.0004	2.1792	0.0012
06YS-4_5.1	12.38	0.18	10.96	0.16	26.80	0.38	0.8865	0.0004	2.1795	0.0012
06YS-4_5.2	12.77	0.18	11.31	0.16	27.67	0.38	0.8867	0.0004	2.1806	0.0012
06YS-4_5.3	13.18	0.18	11.68	0.16	28.58	0.38	0.8868	0.0004	2.1794	0.0012
06YS-4_6.1	8.96	0.18	7.87	0.16	19.19	0.38	0.8827	0.0004	2.1742	0.0012
06YS-4_6.2	10.61	0.18	9.37	0.16	22.87	0.38	0.8856	0.0004	2.1769	0.0012
06YS-4_6.3	11.70	0.18	10.32	0.16	25.28	0.38	0.8854	0.0004	2.1776	0.0012
06YS-4_7.1	10.36	0.18	9.16	0.16	22.36	0.38	0.8866	0.0004	2.1815	0.0012
06YS-4_7.2	13.19	0.18	11.70	0.16	28.60	0.38	0.8873	0.0004	2.1793	0.0012
06YS-4_7.3	9.93	0.18	8.78	0.16	21.40	0.38	0.8861	0.0004	2.1805	0.0012
06YS-4_glass-1	11.41	0.18	10.07	0.16	24.65	0.38	0.8859	0.0004	2.1784	0.0012
06YS-4_glass-2	14.42	0.18	12.79	0.16	31.33	0.38	0.8867	0.0004	2.1801	0.0012

Table 2 continued

Sample	^{206}Pb/^{204}Pb	$\pm 1\sigma$ ext	^{207}Pb/^{204}Pb	$\pm 1\sigma$ ext	^{208}Pb/^{204}Pb	$\pm 1\sigma$ ext	^{207}Pb/^{206}Pb	$\pm 1\sigma$ ext	^{208}Pb/^{206}Pb	$\pm 1\sigma$ ext
06YS-4_glass-3	8.54	0.18	7.53	0.16	18.31	0.38	0.8864	0.0004	2.1796	0.0012
06YS-4_glass-4	11.07	0.18	9.79	0.16	23.90	0.38	0.8868	0.0004	2.1797	0.0012
Tuff of Bluff Point (06YS-2)										
06YS-2_1.1	12.53	0.18	11.09	0.16	27.13	0.38	0.8863	0.0004	2.1796	0.0012
06YS-2_1.2	12.36	0.18	10.95	0.16	26.75	0.38	0.8871	0.0004	2.1793	0.0012
06YS-2_1.3	12.88	0.18	11.40	0.16	27.90	0.38	0.8862	0.0004	2.1797	0.0012
06YS-2_1.4	12.76	0.18	11.30	0.16	27.65	0.38	0.8869	0.0004	2.1809	0.0012
06YS-2_3.1	7.42	0.18	6.53	0.16	15.83	0.38	0.8865	0.0004	2.1804	0.0012
06YS-2_3.2	7.46	0.18	6.56	0.16	15.91	0.38	0.8867	0.0004	2.1798	0.0012
06YS-2_3.3	8.12	0.18	7.16	0.16	17.36	0.38	0.8870	0.0004	2.1786	0.0012
06YS-2_3.4	8.16	0.18	7.19	0.16	17.45	0.38	0.8871	0.0004	2.1793	0.0012
06YS-2_4.1	8.24	0.18	7.26	0.16	17.64	0.38	0.8864	0.0004	2.1796	0.0012
06YS-2_4.2	8.76	0.18	7.72	0.16	18.77	0.38	0.8866	0.0004	2.1779	0.0012
06YS-2_4.3	8.46	0.18	7.47	0.16	18.13	0.38	0.8874	0.0004	2.1793	0.0012
06YS-2_5.1	11.23	0.18	9.92	0.16	24.23	0.38	0.8861	0.0004	2.1779	0.0012
06YS-2_5.2	11.18	0.18	9.89	0.16	24.14	0.38	0.8866	0.0004	2.1789	0.0012
06YS-2_5.3	11.81	0.18	10.45	0.16	25.53	0.38	0.8871	0.0004	2.1790	0.0012
06YS-2_6.1	6.42	0.18	5.57	0.16	13.45	0.38	0.8742	0.0004	2.1495	0.0012
06YS-2_6.2	7.17	0.18	6.29	0.16	15.22	0.38	0.8831	0.0004	2.1696	0.0012
06YS-2_6.3	11.34	0.18	10.01	0.16	24.46	0.38	0.8839	0.0004	2.1755	0.0012
06YS-2_6.4	8.53	0.18	7.46	0.16	18.15	0.38	0.8783	0.0004	2.1623	0.0012
06YS-2_9.1	10.37	0.18	9.17	0.16	22.35	0.38	0.8876	0.0004	2.1795	0.0012
06YS-2_glass-1	8.44	0.18	7.44	0.16	18.07	0.38	0.8868	0.0004	2.1795	0.0012
06YS-2_glass-2	5.37	0.18	4.70	0.16	11.29	0.38	0.8870	0.0004	2.1794	0.0012
06YS-2_glass-3	4.56	0.18	3.95	0.16	9.45	0.38	0.8813	0.0004	2.1668	0.0012
06YS-2_glass-4	5.41	0.18	4.70	0.16	11.34	0.38	0.8837	0.0004	2.1737	0.0012
South Biscuit Basin flow (YL96-2)										
YL96-2_1.1	11.18	0.18	9.90	0.16	24.17	0.38	0.8872	0.0004	2.1811	0.0012
YL96-2_1.2	14.02	0.18	12.44	0.16	30.43	0.38	0.8867	0.0004	2.1786	0.0012
YL96-2_1.3	14.16	0.18	12.55	0.16	30.69	0.38	0.8863	0.0004	2.1779	0.0012
YL96-2_1.4	14.42	0.18	12.80	0.16	31.33	0.38	0.8869	0.0004	2.1782	0.0012
YL96-2_2.1	14.40	0.18	12.77	0.16	31.25	0.38	0.8865	0.0004	2.1769	0.0012
YL96-2_2.2	14.87	0.18	13.17	0.16	32.25	0.38	0.8861	0.0004	2.1770	0.0012
YL96-2_2.3	14.99	0.18	13.28	0.16	32.54	0.38	0.8858	0.0004	2.1768	0.0012
YL96-2_3.1	14.20	0.18	12.56	0.16	30.76	0.38	0.8848	0.0004	2.1745	0.0012
YL96-2_3.2	14.52	0.18	12.86	0.16	31.48	0.38	0.8852	0.0004	2.1739	0.0012
YL96-2_3.3	15.34	0.18	13.59	0.16	33.28	0.38	0.8854	0.0004	2.1747	0.0012
YL96-2_4.1	14.56	0.18	12.90	0.16	31.58	0.38	0.8860	0.0004	2.1757	0.0012
YL96-2_4.2	14.90	0.18	13.22	0.16	32.36	0.38	0.8869	0.0004	2.1778	0.0012
YL96-2_4.3	15.18	0.18	13.45	0.16	32.95	0.38	0.8863	0.0004	2.1773	0.0012
YL96-2_5.1	11.22	0.18	9.92	0.16	24.21	0.38	0.8866	0.0004	2.1778	0.0012
YL96-2_5.2	12.25	0.18	10.85	0.16	26.49	0.38	0.8869	0.0004	2.1778	0.0012
YL96-2_5.3	11.48	0.18	10.15	0.16	24.86	0.38	0.8860	0.0004	2.1751	0.0012
YL96-2_6.1	14.29	0.18	12.66	0.16	30.99	0.38	0.8864	0.0004	2.1772	0.0012
YL96-2_6.2	14.68	0.18	13.03	0.16	31.87	0.38	0.8860	0.0004	2.1770	0.0012
YL96-2_6.3	14.61	0.18	12.95	0.16	31.73	0.38	0.8863	0.0004	2.1779	0.0012
YL96-2_7.1	10.25	0.18	8.98	0.16	21.89	0.38	0.8780	0.0004	2.1578	0.0012
YL96-2_7.2	10.40	0.18	9.18	0.16	22.38	0.38	0.8840	0.0004	2.1724	0.0012

Table 2 continued

Sample	$^{206}Pb/^{204}Pb$	±1σ ext	$^{207}Pb/^{204}Pb$	±1σ ext	$^{208}Pb/^{204}Pb$	±1σ ext	$^{207}Pb/^{206}Pb$	±1σ ext	$^{208}Pb/^{206}Pb$	±1σ ext
YL96-2_7.3	10.89	0.18	9.61	0.16	23.44	0.38	0.8844	0.0004	2.1725	0.0012
YL96-2_8.1	13.25	0.18	11.74	0.16	28.69	0.38	0.8855	0.0004	2.1762	0.0012
YL96-2_8.2	13.78	0.18	12.22	0.16	29.88	0.38	0.8873	0.0004	2.1771	0.0012
YL96-2_8.3	14.12	0.18	12.52	0.16	30.63	0.38	0.8874	0.0004	2.1782	0.0012
Lava Creek Tuff, Member A (LCT-3A)										
LCT-3A_1.1	16.20	0.32	14.57	0.29	36.01	0.72	0.8996	0.0006	2.2298	0.0009
LCT-3A_1.2	16.13	0.32	14.50	0.29	35.84	0.72	0.8989	0.0006	2.2279	0.0009
LCT-3A_1.3	16.66	0.32	14.99	0.29	37.02	0.72	0.8986	0.0006	2.2261	0.0009
LCT-3A_1.4	16.50	0.32	14.85	0.29	36.67	0.72	0.8996	0.0006	2.2273	0.0009
LCT-3A_2.1	16.52	0.32	14.87	0.29	36.79	0.72	0.8998	0.0006	2.2298	0.0009
LCT-3A_2.2	16.68	0.32	15.02	0.29	37.12	0.72	0.9004	0.0006	2.2312	0.0009
LCT-3A_2.3	16.70	0.32	15.03	0.29	37.20	0.72	0.8999	0.0006	2.2299	0.0009
LCT-3A_3.1	16.59	0.32	14.91	0.29	36.87	0.72	0.8992	0.0006	2.2277	0.0009
LCT-3A_3.2	16.75	0.32	15.07	0.29	37.26	0.72	0.8995	0.0006	2.2289	0.0009
LCT-3A_3.3	16.80	0.32	15.14	0.29	37.39	0.72	0.8998	0.0006	2.2293	0.0009
LCT-3A_4.1	16.68	0.32	14.97	0.29	37.01	0.72	0.8972	0.0006	2.2229	0.0009
LCT-3A_4.2	16.80	0.32	15.12	0.29	37.32	0.72	0.8992	0.0006	2.2279	0.0009
LCT-3A_4.3	16.86	0.32	15.19	0.29	37.50	0.72	0.8994	0.0006	2.2283	0.0009
LCT-3A_5.1	16.69	0.32	15.01	0.29	37.12	0.72	0.8997	0.0006	2.2292	0.0009
LCT-3A_5.2	16.77	0.32	15.11	0.29	37.34	0.72	0.9004	0.0006	2.2304	0.0009
LCT-3A_5.3	16.84	0.32	15.17	0.29	37.48	0.72	0.9004	0.0006	2.2306	0.0009
LCT-3A_6.1	16.75	0.32	15.08	0.29	37.27	0.72	0.8999	0.0006	2.2279	0.0009
LCT-3A_6.2	16.74	0.32	15.08	0.29	37.24	0.72	0.9002	0.0006	2.2290	0.0009
LCT-3A_6.3	16.88	0.32	15.18	0.29	37.56	0.72	0.8997	0.0006	2.2281	0.0009
LCT-3A_7.1	16.60	0.32	14.90	0.29	36.74	0.72	0.8959	0.0006	2.2175	0.0009
LCT-3A_7.2	16.75	0.32	15.06	0.29	37.24	0.72	0.8977	0.0006	2.2244	0.0009
LCT-3A_7.3	16.74	0.32	15.03	0.29	37.14	0.72	0.8983	0.0006	2.2249	0.0009
LCT-3A_8.1	17.06	0.32	15.34	0.29	37.93	0.72	0.8988	0.0006	2.2270	0.0009
LCT-3A_8.2	17.05	0.32	15.38	0.29	38.03	0.72	0.9002	0.0006	2.2312	0.0009
LCT-3A_8.3	16.85	0.32	15.18	0.29	37.53	0.72	0.8998	0.0006	2.2293	0.0009
Huckleberry Ridge Tuff, Member B (HRT-1)										
HRT-1_1.1	16.14	0.32	14.65	0.29	35.90	0.72	0.9099	0.0006	2.2361	0.0009
HRT-1_1.2	16.40	0.32	14.94	0.29	36.63	0.72	0.9101	0.0006	2.2372	0.0009
HRT-1_1.3	16.62	0.32	15.13	0.29	37.11	0.72	0.9121	0.0006	2.2405	0.0009
HRT-1_2.1	16.12	0.32	14.64	0.29	35.94	0.72	0.9097	0.0006	2.2359	0.0009
HRT-1_2.2	16.25	0.32	14.78	0.29	36.24	0.72	0.9100	0.0006	2.2366	0.0009
HRT-1_2.3	16.05	0.32	14.63	0.29	35.90	0.72	0.9118	0.0006	2.2391	0.0009
HRT-1_3.1	15.95	0.32	14.52	0.29	35.59	0.72	0.9102	0.0006	2.2356	0.0009
HRT-1_3.2	16.17	0.32	14.73	0.29	36.11	0.72	0.9115	0.0006	2.2392	0.0009
HRT-1_3.3	16.30	0.32	14.82	0.29	36.34	0.72	0.9103	0.0006	2.2364	0.0009
HRT-1_4.1	16.21	0.32	14.75	0.29	36.17	0.72	0.9105	0.0006	2.2376	0.0009
HRT-1_4.2	16.20	0.32	14.75	0.29	36.19	0.72	0.9113	0.0006	2.2401	0.0009
HRT-1_4.3	16.24	0.32	14.78	0.29	36.26	0.72	0.9116	0.0006	2.2422	0.0009
Huckleberry Ridge Tuff, Member C (HRT-C)										
HRT-C_3.1	17.40	0.32	15.18	0.29	36.46	0.72	0.8693	0.0006	2.088	0.0009
HRT-C_3.2	17.47	0.32	15.27	0.29	36.69	0.72	0.8702	0.0006	2.090	0.0009
HRT-C_3.3	17.08	0.32	14.90	0.29	35.78	0.72	0.8695	0.0006	2.089	0.0009
HRT-C_5.1	17.72	0.32	15.44	0.29	37.09	0.72	0.8682	0.0006	2.085	0.0009

Table 2 continued

Sample	$^{206}Pb/^{204}Pb$	$\pm1\sigma$ ext	$^{207}Pb/^{204}Pb$	$\pm1\sigma$ ext	$^{208}Pb/^{204}Pb$	$\pm1\sigma$ ext	$^{207}Pb/^{206}Pb$	$\pm1\sigma$ ext	$^{208}Pb/^{206}Pb$	$\pm1\sigma$ ext
HRT-C_5.2	17.79	0.32	15.49	0.29	37.23	0.72	0.8690	0.0006	2.086	0.0009
HRT-C_5.3	17.71	0.32	15.44	0.29	37.10	0.72	0.8688	0.0006	2.086	0.0009
HRT-C_6.1	17.56	0.32	15.30	0.29	36.74	0.72	0.8682	0.0006	2.085	0.0009
HRT-C_6.2	17.58	0.32	15.31	0.29	36.76	0.72	0.8676	0.0006	2.084	0.0009
HRT-C_6.3	17.70	0.32	15.42	0.29	37.03	0.72	0.8679	0.0006	2.083	0.0009
HRT-C_7.1	14.30	0.32	12.44	0.29	29.89	0.72	0.8682	0.0006	2.088	0.0009
HRT-C_7.2	16.96	0.32	14.79	0.29	35.55	0.72	0.8697	0.0006	2.090	0.0009
HRT-C_7.3	15.59	0.32	13.56	0.29	32.63	0.72	0.8677	0.0006	2.090	0.0009
HRT-C_8.1	16.87	0.32	15.20	0.29	37.36	0.72	0.9017	0.0006	2.221	0.0009
HRT-C_8.2	16.95	0.32	15.29	0.29	37.59	0.72	0.9020	0.0006	2.221	0.0009
HRT-C_8.3	16.86	0.32	15.21	0.29	37.38	0.72	0.9016	0.0006	2.220	0.0009
HRT-C_9.1	17.49	0.32	15.24	0.29	36.63	0.72	0.8691	0.0006	2.088	0.0009
HRT-C_10.1	18.22	0.32	15.81	0.29	37.94	0.72	0.8647	0.0006	2.073	0.0009
HRT-C_11.1	18.01	0.32	15.67	0.29	37.63	0.72	0.8671	0.0006	2.082	0.0009
HRT-C_12.1	17.78	0.32	15.50	0.29	37.25	0.72	0.8694	0.0006	2.088	0.0009

Uncertainties of Pb isotope ratios are $\pm1\sigma$ external errors for a NIST 612 glass standard (Baker et al. 2004)

We note that HRT-C grain 8 is an outlier and not included in Fig. 6a

2010; Pritchard and Larson in review). Our new Pb isotope data represent a departure from prior work in that they were acquired for single sanidine crystals, rather than whole-rock or glass averages, and with a different technique, LA-ICP-MS for single spot analyses rather than TIMS for bulk analyses. More high-resolution single crystal analyses are needed for detailed assessments of radiogenic source components in Yellowstone magmas. However, using our existing sanidine lead isotope dataset, we are able to make several important observations about CPM rhyolites in the context of published radiogenic isotope datasets: (1) Compared to individual tuff members of Yellowstone's caldera-forming eruptions, post-caldera CPM rhyolites define a larger range in radiogenic isotope space, (2) The CPM array is unique and does not overlap any of the established radiogenic isotope fields for Yellowstone rhyolites or basalts, (3) Crystals within CPM rhyolites have heterogeneous radiogenic isotope composition that become progressively more homogenous in younger units, and (4) A significant proportion of CPM crystals have radiogenic isotope compositions that are characteristic of UBM rather than CPM units.

Thermometry of analyzed rhyolites

We determined zircon saturation temperatures and liquidus temperatures for all analyzed rhyolites and synthesized this new data with temperature data published by Bindeman and Valley (2001) and Vazquez et al. (2009) (Fig. 7). When temperatures are plotted against melt $\delta^{18}O$ values for individual UBM units, we find that they have similar oxygen isotope compositions and temperature ranges ($\sim$820–900°C) and that the oldest and most primitive ($\sim$70 wt% SiO_2) East Biscuit Basin flow also has the highest liquidus temperature ($\sim$940°C; Fig. 7a). Temperatures and melt $\delta^{18}O$ values for CPM rhyolites are more variable than UBM rhyolites, with temperatures that range from $\sim$750 to 900°C (Fig. 7a). We observe a trend of decreasing temperature with increasing melt $\delta^{18}O$ values for CPM rhyolites, but the temperature ranges for individual CPM units are often quite large due to discrepancies between the different geothermometers. Therefore, we interpret this trend with caution; more precise thermometry data are needed before this trend can be confirmed or refuted.

When temperatures of CPM rhyolites are plotted against their eruption ages (Fig. 7b), it appears that they become progressively cooler through time. Vazquez et al. (2009) first described this trend using a smaller dataset that is now synthesized with our new data in Fig. 7b. Using a cumulative eruptive volume curve constructed with published eruptive volumes and eruption ages for CPM units (Christiansen et al. 2007), we observe an inverse correlation between temperature and eruptive volume (Fig. 7b). A spike in the cumulative eruptive volume curve, following eruption of the very voluminous 114-ka West Yellowstone flow, marks the point at which temperatures of CPM rhyolites begin to decrease. However, as noted previously, the large temperature ranges between the various thermometers and their inherent uncertainties warrant caution in these observations.
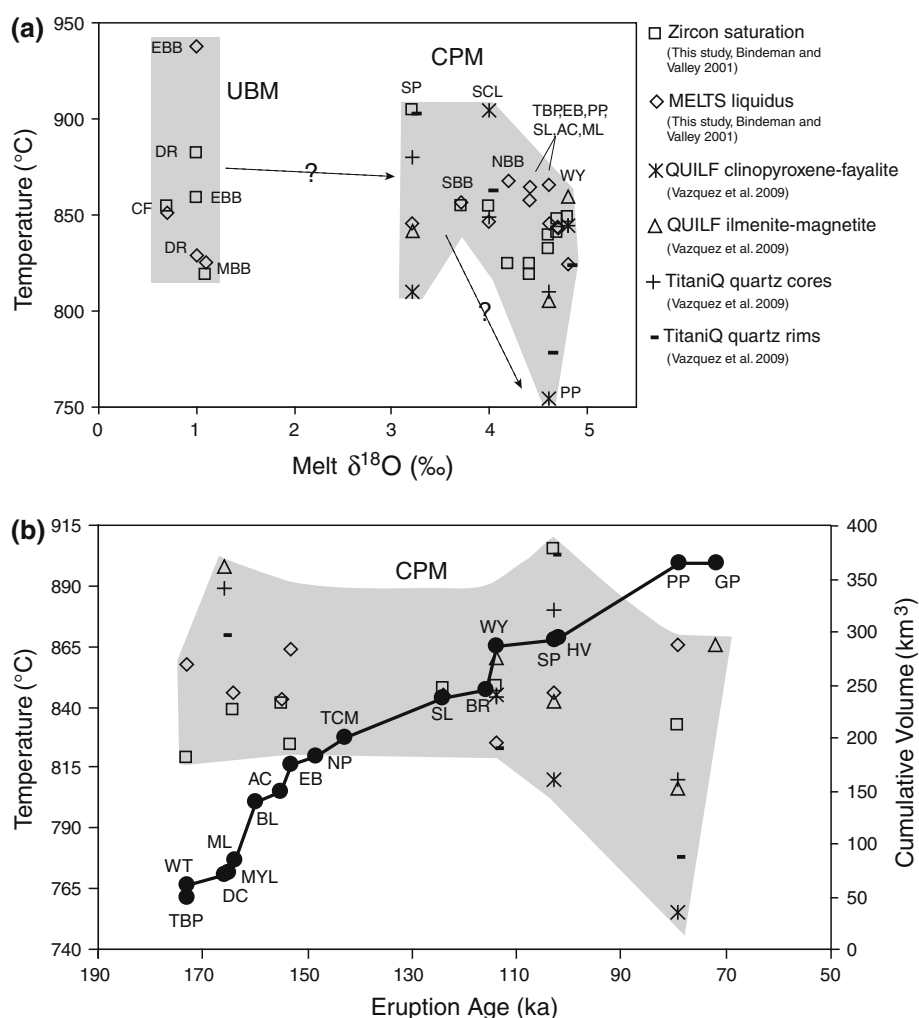
Fig. 7 **a** Temperatures of Upper Basin Member (UBM) and Central Plateau Member (CPM) rhyolites plotted against melt $\delta^{18}O$ values. *Symbols* show the temperatures derived from different thermometry datasets, synthesized from Bindeman and Valley (2001), Vazquez et al. (2009) and this study (see Supplementary Material 3 for temperature data). Melt $\delta^{18}O$ values are taken from Bindeman and Valley (2001), Bindeman et al. (2008) and this study. Temperature-melt $\delta^{18}O$ fields for UBM and CPM rhyolites are *shaded*. Unit abbreviations are the same as those used in Fig. 5. We tentatively indicate a trend of decreasing temperatures with increasing melt $\delta^{18}O$ values (*dashed arrows*); however, the temperature ranges for individual units are often quite large, making this trend difficult to confirm. **b** Temperature and cumulative eruptive volume of Central Plateau Member (CPM) rhyolites plotted against eruption age. Thermometry symbols are the same as those used in **a**. Volumes and eruption ages are from Christiansen et al. (2007). The cumulative eruptive volume curve is shown as a *black line* connected by individual units (*black circles*). Unit abbreviations are the same as those used in Fig. 5, with the addition of CPM units West Thumb flow (WT), Dry Creek flow (DC), Mary Lake flow (MYL), Buffalo Lake flow (BL), Nez Perce Creek flow (NP), Tuff of Cold Mountain Creek (TCM), Bechler River flow (BC), Hayden Valley flow (HV), and Grants Pass flow (GP). Note that the temperature curve is negatively correlated with the cumulative eruptive volume curve for CPM rhyolites, interpreted here as cooling of the CPM magma reservoir as eruptions proceeded in the Yellowstone caldera

Discussion

In the following discussion, we focus on our new age (U–Th and U–Pb) and isotopic (O and Pb) data for post-LCT rhyolites of the Yellowstone caldera. We synthesize our new data with previously published age and geochemical datasets for post-LCT rhyolites to create a unified model of magma genesis. Our discussion is subdivided into three main parts: (1) Model of post-LCT (UBM and CPM) magma genesis, (2) Petrologic, thermal, and temporal

considerations for CPM magmas, and (3) Similarities and differences between CPM magmas and voluminous late-stage magmas of the pre-Yellowstone Heise volcanic field.

Model of post-LCT magma genesis

Our new age and isotopic datasets for CPM rhyolites require several key changes to published post-LCT magma genesis models (Bindeman and Valley 2000, 2001; Vazquez and Reid 2002; Bindeman et al. 2008). The most

salient new result of this study is that unlike UBM rhyolites, which were generated from independent parcels of melt with unique oxygen isotopic compositions (Bindeman et al. 2008), many of the voluminous CPM rhyolites have more homogeneous oxygen isotopic compositions that permit derivation from a common magma source. There are notable exceptions to this rule, for instance the Scaup Lake flow, South Biscuit Basin flow, and Solfatara Plateau flow. However, as we discuss below, the ∼260-ka Scaup Lake and South Biscuit Basin flows retain important age and isotopic information about the early stages of CPM magma assembly prior to the loss of crystal evidence by convection and homogenization of a large CPM magma reservoir. We discuss our new model for post-LCT magma genesis chronologically, starting with discussion of the early UBM rhyolite eruptions (∼520–470 ka) followed by discussion of the later (∼260–75 ka) CPM rhyolite eruptions.

Previous studies of UBM rhyolites (Canyon flow, Dunraven Road flow, Middle Biscuit Basin flow) have shown that they contain a large proportion of zircon xenocrysts with ages and normal-δ^{18}O values that correspond to HRT, LCT, and pre-LCT units (Bindeman et al. 2001, 2008). These zircons are not in oxygen isotopic equilibrium with their host low-δ^{18}O melts and provide evidence for wholesale remelting of hydrothermally altered (^{18}O-depleted in the groundmass) intracaldera rocks of HRT, LCT, and pre-LCT protoliths (Bindeman et al. 2008; Fig. 8). Our new results for the East Biscuit Basin flow indicate that like other UBM units, it contains zircons with a broad age spectrum and normal-δ^{18}O values that are not in equilibrium with the low-δ^{18}O host melt; however, unlike other UBM units, East Biscuit Basin flow does not contain any zircons with low-δ^{18}O values or younger (eruption) ages. The East Biscuit Basin flow also has a unique mineralogy and major and trace element geochemistry relative to other UBM units, for instance its lack of sanidine and quartz, lower-silica composition, and higher Sr concentration, indicating that it was the first, most primitive rhyolite to erupt with the Yellowstone caldera (Girard and Stix 2009). Thermometry results for the East Biscuit Basin flow show that it also had the hottest liquidus temperature of any post-LCT rhyolite (Fig. 7a). Our new zircon data indicate that the East Biscuit Basin flow was generated by rapid remelting of pre-LCT intracaldera protoliths and erupted before a new phase of (low-δ^{18}O) zircon saturation and crystallization.

Like UBM rhyolites, the ∼260-ka Scaup Lake flow has a heterogeneous zircon population with δ^{18}O values that are out of equilibrium with the low-δ^{18}O host melt (Bindeman et al. 2008). Disequilibrium textures of major phenocryst phases, less-evolved mineral and whole-rock geochemistry, and a lower whole-rock Rb/Sr ratio set this

unit apart from other CPM rhyolites (Vazquez and Reid 2002; Vazquez et al. 2009; Girard and Stix 2010). Zircons from the South Biscuit Basin flow have comparably heterogeneous δ^{18}O values, and both units have zircon cores with the distinctive low-δ^{18}O signature of UBM rhyolites, suggesting that they represent remelts of intracaldera UBM intrusions (Bindeman et al. 2008). Our new Pb isotope data reveal that South Biscuit Basin flow also contains sanidine crystals that are compositionally more similar to UBM rather than CPM rhyolites (Fig. 6). Mineral and whole-rock geochemistry of the Scaup Lake flow and South Biscuit Basin flow are nearly identical and define a unique end member composition of CPM rhyolite eruptions (Girard and Stix 2010). Taking this combined evidence into account, we suggest that the Scaup Lake and South Biscuit Basin flows are important bridging links between the UBM and CPM eruptions, representing the oldest, least-evolved CPM magma batches that retain a genetic connection to the plutonic UBM protoliths that sourced them (Fig. 8).

Younger CPM units (Pitchstone Plateau flow, West Yellowstone flow, Elephant Back flow, Tuff of Bluff Point and North Biscuit Basin flow) are distinctly more homogenous in their zircon δ^{18}O values and have mineral assemblages that are in oxygen isotopic equilibrium with low-δ^{18}O groundmass glasses. Our data indicate that these CPM units were derived from batch assembly and homogenization of heterogeneous pockets of low-δ^{18}O melts, such as the older Scaup Lake and South Biscuit Basin flows, which tapped UBM intrusions (Fig. 8). The fact that CPM rhyolites have zircon populations that fall within a narrow δ^{18}O range that approximates the homogenized UBM zircon average (Fig. 5a) supports this interpretation. Furthermore, several CPM units dated by us (Tuff of Bluff Point, Elephant Back flow and North Biscuit Basin flow) and some of those dated by Vazquez and Reid (2002) (Pitchstone Plateau flow, Solfatara Plateau flow, West Yellowstone flow and Dry Creek flow) have older zircon crystals with ∼250–300 ka ages that match those of the Scaup Lake and South Biscuit Basin flows. In addition to zircon crystal evidence for a link between UBM and CPM magmas, we also find that a subset of sanidine crystals within the Tuff of Bluff Point and Elephant Back flow point to a UBM rather than CPM heritage (Fig. 6).

Similar to observations made using whole-rocks and phenocrysts of post-LCT rhyolites for progressively more-evolved, more-juvenile, and cooler CPM magmas through time (Hildreth et al. 1984, 1991; Vazquez et al. 2009; Girard and Stix 2010), our new isotope and age data for single crystals demonstrate that younger CPM rhyolites tend to have less heterogeneous zircon age populations (Fig. 3), slightly higher average zircon δ^{18}O values (Fig. 4), and less heterogeneous, but more-juvenile sanidine lead isotope compositions (Fig. 6). Taken together,

Fig. 8 Schematic model of rhyolite genesis at Yellowstone caldera. Eruption of the Lava Creek Tuff 640 ka caused collapse of the Yellowstone caldera, bringing intracaldera Huckleberry Ridge Tuff (HRT) and Lava Creek Tuff (LCT) rocks in contact with unerupted LCT magma. Hydrothermal circulation cells formed in the intracaldera block, altering rocks with low-δ^{18}O meteoric fluids. Intracaldera intrusions of unerupted LCT magma caused resurgent doming in the Yellowstone caldera, forming the Mallard Lake and Sour Creek resurgent domes. Melting of intracaldera intrusions and intracaldera rocks formed independent batches of low-δ^{18}O magma that erupted ~520–470 ka near the Mallard Lake and Sour Creek domes (Upper Basin Member rhyolites). Melting of intracaldera intrusions, intracaldera rocks, and Upper Basin Member plutonic remnants formed primitive Central Plateau Member rhyolite batches ~260 ka (South Biscuit Basin (SBB) and Scaup Lake (SCL) flows). The locus of melting expanded in the intracaldera block, and independent rhyolite batches accreted to form a large-volume, low-δ^{18}O magma reservoir that sourced Central Plateau Member eruptions ~170–75 ka, producing the Tuff of Bluff Point (TBP), Elephant Back flow (EB), North Biscuit Basin flow (NBB), West Yellowstone flow (WY), and Pitchstone Plateau flow (PP). Eruptions became progressively more homogeneous, more evolved, and cooler through time. Disparate geochemical data for the Solfatara Plateau flow (SP) indicate that it was derived from an independent magma batch

Petrologic, thermal, and temporal considerations for CPM eruptions

The sequential nature of CPM rhyolite eruptions and detailed constraints on eruption ages and eruptive volumes for CPM units (Christiansen et al. 2007) make it possible to evaluate magma genesis from the onset of eruptions ~260 ka to the last most evolved eruption ~75 ka. In this section, we discuss petrologic, thermal, and temporal considerations for the model of post-LCT magma genesis presented in the previous section.

The earliest erupted CPM rhyolites, the ~260-ka Scaup Lake and South Biscuit Basin flows, define the least-evolved end member composition of CPM rhyolite eruptions in terms of common fractionation indices such as Al_2O_3 (plagioclase and sanidine), TiO_2 (Fe–Ti oxides), Rb/Sr (plagioclase and sanidine), and Zr/Nb (zircon; see Supplementary Material 5). We estimate ~25–30% fractional crystallization (30% plagioclase, 60% sanidine, 10% quartz) to derive the youngest and most evolved Pitchstone Plateau flow from the more-evolved Scaup Lake and South Biscuit Basin flows (see Supplementary Material 6 for fractional crystallization calculations). We note that this estimate is significantly less than the original estimate of >40% fractional crystallization by Vazquez and Reid (2002), which was based on a higher Rb/Sr ratio that is revised to a lower ratio in Vazquez et al. (2009). In addition to the geochemical disparities between old and young CPM rhyolites, distinct petrographic differences are also apparent. Disequilibrium mineral textures are commonly observed in thin sections of the Scaup Lake and South Biscuit Basin flows, indicating incomplete dissolution of

this evidence indicates that the CPM rhyolites tapped an evolving magma reservoir in which antecrystic and xenocrystic heterogeneity of discrete magma batches was progressively annealed by convection, homogenization, and dissolution–reprecipitation (Fig. 8). Subtle isotopic differences in younger units suggest open-system processes such as assimilation and recharge within the differentiating CPM magma chamber.

crystals, whereas progressively younger CPM units have more euhedral phenocrysts with fewer disequilibrium mineral textures (see Supplementary Material 2 for photomicrographs).

If younger CPM rhyolites were indeed assembled from batches of early CPM magmas, like the Scaup Lake and South Biscuit Basin flows, crystal dissolution would have had to have been complete by the time of eruption of the Tuff of Bluff Point, North Biscuit Basin flow, and Elephant Back flow ($\sim$170–155 ka), which have distinct and homogeneous zircon ages and O isotope compositions relative to the earliest CPM eruptions (Fig. 5a). For a liquidus temperature of 850°C and a Zr undersaturation of 40 ppm, $\sim$30 ky is required for complete dissolution of a spherical zircon phenocryst 100 µm in diameter (Watson 1996). This time requirement is consistent with the $\geq$90 ky age gap between early ($\sim$260 ka) and late ($\sim$170–75 ka) CPM eruptions. Based on the exceptionally large cumulative eruptive volume of CPM rhyolites ($>$600 km^3), batch assembly would have had to proceed at a rate of at least 3–4 km^3/ky. Assuming basalt can melt 1–2 times the volume of rhyolite,[1] this corresponds to a basaltic input rate of 1–4 km^3/ky. Interestingly, this assembly process seems to have been thermally buffered until $\sim$110 ka, based on the similarity of thermometry results for CPM rhyolites up until this point (Fig. 7b). After the eruption of the very voluminous West Yellowstone flow (41 km^3), CPM magmas appear to become cooler through time (Fig. 7b). If this trend is real (despite the significant spread in the compiled thermometry data), then this may mark the point in time at which batch assembly stopped beneath the Yellowstone caldera. In this scenario, the negative correlation between cumulative eruptive volume and temperature reflects cooling of the assembled CPM magma reservoir as recorded by sequential rhyolite eruptions. The youngest Pitchstone Plateau flow represents one of the last (and largest) extractions of magma from this assembled source.

Analogy between CPM eruptions and voluminous late-stage magmas of the extinct Heise supervolcano

The Heise caldera complex in eastern Idaho is Yellowstone's most immediate predecessor in the Yellowstone hot spot track (Pierce and Morgan 1992). By analogy with Yellowstone, the terminal stage of caldera cluster evolution at Heise produced the large-volume ($>$1,800 km^3) low-δ^{18}O Kilgore Tuff and post-Kilgore rhyolites, comparable in timing, magnitude of δ^{18}O depletion and cumulative eruptive volume to the CPM phase of rhyolitic eruptions at Yellowstone (Watts et al. 2011). While individual Kilgore Tuff zircons exhibit a wide range in δ^{18}O values, from -1.3 to 6.1‰, bulk zircon and less refractory phenocrysts phases of quartz and sanidine have homogeneous δ^{18}O values that correspond to a low-δ^{18}O magma value of 3.4 ± 0.1‰ for samples erupted $>$100 km apart, providing a compelling case for batch assembly and homogenization of heterogeneous melts on a caldera-wide scale prior to the Kilgore Tuff eruption (Watts et al. 2011).

In comparison, most CPM rhyolites are homogeneous in δ^{18}O even on the single crystal scale, with average zircon values that fall within a narrow low-δ^{18}O range of 2.7–2.8‰ (Figs. 4, 5a). However, the oldest CPM rhyolites, the South Biscuit Basin and Scaup Lake flows, exhibit much greater zircon heterogeneity (Fig. 5a). We propose that the homogenization through time effect that we observe for CPM rhyolites (Fig. 5a), whereby they become progressively more homogeneous and retain fewer inherited crystals in younger eruptions, is an expected outcome for caldera cluster evolution: heterogeneities of the intracaldera block are progressively annealed by successive episodes of bulk remelting. While at Yellowstone, these late-stage magmas erupted as sequential "snapshots" over the past 260 ky, the Kilgore Tuff erupted in a single, climactic pulse that tapped an assembled, but not fully annealed, magma chamber.

Concluding remarks

The results of the present study provide high-resolution, crystal scale insights into magma genesis under one of the world's largest supervolcanoes. This study builds on previous studies of Yellowstone and pre-Yellowstone supereruptions in the Yellowstone hotspot track that reveal diverse paths of large-volume rhyolite genesis. In some cases, magma accumulation leads to the formation of a large isotopically and chemically homogeneous magma reservoir, with few zircon xenocrysts of diverse δ^{18}O compositions (e.g., Yellowstone's MFT and LCT), while in other cases, significant zircon δ^{18}O heterogeneity persists even after segregation of $>$1,800 km^3 of magma, as in the case of Heise's Kilgore Tuff.

Our study of voluminous CPM lavas reveals the anatomy of a failed supereruption. With their young ages that permit detailed U-Th zircon geochronology, CPM lavas can be used to gain insight into crystal scale records of large silicic magmatic systems. Based on the results of our

---

[1] This calculation is based on 1.5 kJ/kg K heat capacity of basalt, cooling from 1,250°C liquidus to 550°C ambient temperature, with 400 kJ/kg latent heat of crystallization, assuming it is rapidly quenched and 100% crystalline (diabase) with a 40% heat transfer efficiency (Dufek and Bergantz 2005), yielding 580 kJ/kg. To melt a rhyolitic rock by 50%, heating from 550°C ambient temperature to 850°C liquidus, with 0.7 kJ/kg K heat capacity and 300 kJ/kg latent heat of fusion would require 360 kJ/kg. Thus, under the specified conditions, basalt can melt 1–2 times the volume of rhyolite.

present study, it appears that progressive stages of >600 km^3 of rhyolitic magma accumulation occurred from ~ 260 to 155 ka beneath the Yellowstone caldera. This time was sufficiently long to form a homogenous and voluminous magma reservoir that began cooling and erupting large-volume rhyolitic lavas. Annealing of the preexisting crystal cargo, including diverse zircon, quartz, and sanidine crystals, proceeded until all age and isotopic evidence of inheritance was lost by the time of the most evolved and coolest rhyolite eruption ~ 75 ka.

Given that voluminous CPM lavas are low-δ^{18}O rhyolites with isotopic and age evidence for a genetic connection to buried intracaldera volcanic and plutonic rocks from previous eruptions, we speculate that the evolution of caldera volcanism from the Yellowstone caldera block is complete. The remelting of rocks from the uppermost, fusible parts of crust signifies a terminal stage of caldera cluster evolution. These final eruptions provide crystal scale records of a dying magmatic cycle rather than a newly formed or rejuvenated magma chamber. If we can use Heise as a guide, where about 2.5 million years elapsed between the final Kilgore caldera cycle and the onset of eruptions at Yellowstone, more than 2 million years of heating, melting, assembling, and distilling thousands of km^3 of high-silica rhyolite are necessary for renewed supereruptions in the hotspot track. Our in-depth study of isotopic and age variations in single crystals may shed light on similar processes occurring in large caldera centers elsewhere on Earth, and perhaps provide a viable approach for their investigation.

References

Bacon CR, Lowenstern JB (2005) Late Pleistocene granodiorite source for recycled zircon and phenocrysts in rhyodacite lava at Crater Lake, Oregon. Earth Planet Sci Lett 233:277–293

Baker J, Peate D, Waight T, Meyzen C (2004) Pb isotopic analysis of standards and samples using a ^{207}Pb–^{204}Pb double spike and thallium to correct for mass bias with double-focusing MC-ICP-MS. Chem Geol 211:275–303

Barth AP, Wooden JL (2010) Coupled elemental and isotopic analyses of polygenetic zircons from granitic rocks by ion microprobe, with implications for melt evolution and the sources of granitic magmas. Chem Geol 277:149–159

Bindeman IN, Valley JW (2000) The formation of low-δ^{18}O rhyolites after caldera collapse at Yellowstone, Wyoming, USA. Geology 28:719–722

Bindeman IN, Valley JW (2001) Low-δ^{18}O rhyolites from Yellowstone: Magmatic evolution based on analyses of zircons and individual phenocrysts. J Petrol 42:1491–1517

Bindeman IN, Valley JW (2002) Oxygen isotope study of the Long Valley magma system, California: isotope thermometry and convection in large silicic magma bodies. Contrib Mineral Petrol 144:185–205

Bindeman IN, Valley JW, Wooden JL, Persing HM (2001) Post-caldera volcanism: in situ measurement of U-Pb age and oxygen isotope ratio in Pleistocene zircons from Yellowstone caldera. Earth Planet Sci Lett 189:197–206

Bindeman IN, Fu B, Kita NT, Valley JW (2008) Origin and evolution of Yellowstone silicic magmatism based on ion microprobe analysis of isotopically-zoned zircons. J Petrol 49:163–193

Charlier BLA, Wilson CJN, Lowenstern JB, Blake S, van Calsteren PW, Davidson JP (2005) Magma generation at a large, hyperactive silicic volcano (Taupo, New Zealand) revealed by U/Th and U/Pb systematics in zircons. J Petrol 46:3–32

Christiansen RL (2001) The quaternary and Pliocene Yellowstone Plateau volcanic field of Wyoming, Idaho, and Montana. USGS Prof Paper 729-G, 45 pp

Christiansen RL, Lowenstern JB, Smith RB, Heasler H, Morgan LA, Nathansen M, Mastin LG, Muffler LJP, Robinson JE (2007) Preliminary assessment of volcanic and hydrothermal hazards in Yellowstone National Park and vicinity. USGS Open-File Report 1071 2007, 94 pp

Doe BR, Leeman WP, Christiansen RL, Hedge CE (1982) Lead and strontium isotopes and related trace elements as genetic tracers in the Upper Cenozoic rhyolite-basalt association of the Yellowstone Plateau volcanic field. J Geophys Res 87:4785–4806

Dufek J, Bergantz GW (2005) Lower crustal magma genesis preservation: a stochastic framework for the evaluation of basalt–crust interaction. J Petrol 46:2167–2195

Folkes CB, de Silva SL, Schmitt AK, Cas RAF (2011) A reconnaissance of U–Pb zircon ages in the Cerro Galan system, NW Argentina: prolonged magma residence, crystal recycling, and crustal assimilation. J Volcanol Geotherm Res 206:136–147

Friedman I, Lipman PW, Obradovich JD, Gleason JD, Christiansen RL (1974) Meteoric water in magmas. Science 184:1069–1072

Gansecki CA, Mahood GA, McWilliams MO (1996) ^{40}Ar/^{39}Ar geochronology of rhyolites erupted following collapse of the Yellowstone caldera, Yellowstone Plateau volcanic field: implications for crustal contamination. Earth Planet Sci Lett 142:91–107

Ghiorso MS, Sack RO (1995) Chemical mass-transfer in magmatic processes IV: a revised and internally-consistent thermodynamic model for the interpolation and extrapolation of liquid-solid equilibria in magmatic systems at elevated temperatures and pressures. Contrib Mineral Petrol 119:197–212

Girard G, Stix J (2009) Magma recharge and crystal mush rejuvenation associated with early post-collapse Upper Basin Member rhyolites, Yellowstone caldera, Wyoming. J Petrol 50:2095–2125

Girard G, Stix J (2010) Rapid extraction of discrete magma batches from a large differentiating magma chamber: the Central Plateau Member rhyolites, Yellowstone Caldera, Wyoming. Contrib Mineral Petrol 160:441–465

Hildreth W, Christiansen RL, O'Neil JR (1984) Catastrophic isotopic modification of rhyolitic magma at times of caldera subsidence, Yellowstone Plateau Volcanic Field. J Geophys Res 89:8339–8369

Hildreth W, Halliday AN, Christiansen RL (1991) Isotopic and chemical evidence concerning the genesis and contamination of

basaltic and rhyolitic magmas beneath the Yellowstone Plateau Volcanic Field. J Petrol 32:63–138

Kent AJR (2008) In situ analysis of Pb isotope ratios using laser ablation MC-ICP-MS: Controls on precision and accuracy and comparison between Faraday cup and ion counting systems. J Anal Atom Spect 23:968–975

Kita NT, Ushikubo T, Fu B, Valley JW (2009) High precision SIMS oxygen isotope analysis and the effect of sample topography. Chem Geol 264:43–57

Lanphere MA, Champion DE, Christiansen RL, Izett GA, Obradovich JD (2002) Revised ages for tuffs of the Yellowstone Plateau volcanic field: assignment of the Huckleberry Ridge Tuff to a new geomagnetic polarity event. Geol Soc Amer Bull 114:559–568

Obradovich JD (1992) Geochronology of the Late Cenozoic volcanism of Yellowstone National Park and adjoining areas, Wyoming and Idaho. USGS Open-File Report 92–408:1–45

Paces JB, Miller JD (1993) Precise U-Pb ages of Duluth Complex and related mafic intrusions, northeastern Minnesota: geochronological insights to physical, petrogenetic, paleomagnetic, and tectonomagmatic processes associated with the 1.1 Ga Midcontinent Rift System. J Geophys Res 98:13997–14013

Pierce KL, Morgan LA (1992) The track of the Yellowstone hotspot: volcanism, faulting, and uplift. In: Link PK, Kuntz MA, Platt LB (eds) Regional geology of Eastern Idaho and Western Wyoming. Geol Soc Amer Mem 179:1–53

Putirka KD, Tepley FJ (eds) (2008) Minerals, inclusions and volcanic processes. Rev Mineral 69:674

Schmitt AK, Grove M, Harrison TM, Lovera O, Hulen JB, Walters M (2003) The Geysers-Cobb mountain magma system California (Part 1): U-Pb zircon ages of volcanic rocks conditions of zircon crystallization and magma residence times. Geochim Cosmochim Acta 67:3423–3442

Schmitt AK, Stockli DF, Hausback BP (2006) Eruption and magma crystallization ages of Las Tres Vírgenes (Baja California) constrained by combined ^{230}Th/^{238}U and (U–Th)/He dating of zircon. J Volcanol Geotherm Res 158:281–295

Taylor HP (1986) Igneous rocks: II. Isotopic case studies of circumpacific magmatism. In: Valley JW, Taylor Jr HP, O'Neil JR (eds) Stable isotopes in high temperature geological processes. Mineral Soc Am Rev Mineral 16:273–316

Valley JW (2003) Oxygen isotopes in zircon. In: Hanchar JM, Hoskin PWO (eds) Zircon. Mineral Soc Am Rev Mineral 53:343–385

Vazquez JA, Reid MR (2002) Time scales of magma storage and differentiation of voluminous high-silica rhyolites at Yellowstone caldera, Wyoming. Contrib Mineral Petrol 144:274–285

Vazquez JA, Reid MR (2004) Probing the accumulation history of the voluminous Toba magma. Science 305:991–994

Vazquez JA, Kyriazis SF, Reid MR, Sehler RC, Ramos FC (2009) Thermochemical evolution of young rhyolites at Yellowstone: evidence for a cooling but periodically replenished postcaldera magma reservoir. J Volcanol Geotherm Res 188:186–196

Watson EB (1996) Dissolution, growth and survival of zircons during crustal fusion: kinetic principles, geological models and implications for isotopic inheritance. Transactions of the Royal Society of Edinburgh: Earth Sciences 87:43–56

Watson EB, Harrison TM (1983) Zircon saturation revisited: temperature and compositional effects in a variety of crustal magma types. Earth Planet Sci Lett 64:295–304

Watts KE, Leeman WP, Bindeman IN, Larson PB (2010) Supereruptions of the Snake River Plain: two-stage derivation of low-δ^{18}O rhyolites from normal-δ^{18}O crust as constrained by Archean xenoliths. Geology 38:503–506

Watts KE, Bindeman IN, Schmitt AK (2011) Large-volume rhyolite genesis in caldera complexes of the Snake River Plain: Insights from the Kilgore Tuff of the Heise volcanic field Idaho with comparison to Yellowstone and Bruneau-Jarbidge rhyolites. J Petrol 52:857–890

Wiedenbeck M, Allé P, Corfu F, Griffin WL, Meier M, Oberli F, von Quadt A, Roddick JC, Spiegel W (1995) Three natural zircon standards for U-Th-Pb, Lu-Hf, trace element and REE analyses. Geostand Newslett 19:1–23